

Accepted for Publication in *The Astronomical Journal*

A Study of Nine High-Redshift Clusters of Galaxies: IV. Photometry and Spectra of Clusters 1324+3011 and 1604+4321

Marc Postman

Space Telescope Science Institute¹, 3700 San Martin Drive, Baltimore, MD 21218

Electronic mail: postman@stsci.edu

Lori M. Lubin^{2,3}

Palomar Observatory, California Institute of Technology, Pasadena, CA 91125

Electronic mail: lml@pha.jhu.edu

J. B. Oke

Palomar Observatory, California Institute of Technology, Pasadena, CA 91125

and

Dominion Astrophysical Observatory, 5071 W. Saanich Road, Victoria, BC V9E 2E7

Electronic mail: Bev.Oke@nrc.ca

¹Space Telescope Science Institute is operated by the Association of Universities for Research in Astronomy, Inc., under contract to the National Aeronautics and Space Administration.

²Hubble Fellow

³Current address : Department of Physics and Astronomy, Johns Hopkins University, Baltimore, MD 21218

ABSTRACT

New photometric and spectroscopic observations of galaxies in the directions of three distant clusters are presented as part of our on-going high-redshift cluster survey. The clusters are CL1324+3011 at $z = 0.76$, CL1604+4304 at $z = 0.90$, and CL1604+4321 at $z = 0.92$. We have spectroscopically confirmed cluster membership for 20 to 40 galaxies in each system and have also obtained spectra for over 280 field galaxies spanning the range $0 < z < 2.5$. Kinematic estimates of the mass within the central $770h_{65}^{-1}$ kpc of each cluster are in excess of $8 \times 10^{14} h_{65}^{-1} M_{\odot}$. The observed x-ray luminosities in these clusters are at least a factor of 3 smaller than those observed in clusters with similar velocity dispersions at $z \leq 0.4$.

These clusters contain a significant population of elliptical-like galaxies, although these galaxies are not nearly as dominant as in massive clusters at $z \leq 0.5$. We also find a large population of blue cluster members. Defining an active galaxy as one in which the rest equivalent width of [OII] is greater than 15Å, the fraction of active cluster galaxies, within the central $1.0 h_{65}^{-1}$ Mpc, is 45%. In the field population, we find that 65% of the galaxies with redshifts between $z = 0.40$ and $z = 0.85$ are active, while the fraction is 79% for field galaxies at $z > 0.85$. The star formation rate normalized by the rest AB B -band magnitude, SFRN, increases as the redshift increases at a given evolving luminosity. At a given redshift, however, SFRN decreases linearly with increasing luminosity indicating a remarkable insensitivity of the star formation rate to the intrinsic luminosity of the galaxy over the range $-18 \geq ABB \geq -22$. Cluster galaxies in the central $1h_{65}^{-1}$ Mpc regions exhibit depressed star formation rates and contain a larger fraction of galaxies with “ k ” type spectra. The star formation rates in galaxies lying between $1 - 2.5h_{65}^{-1}$ Mpc from the cluster centers, however, are in good agreement with that in galaxies in the general field at similar redshifts. The spectroscopic and photometric properties of the cluster galaxies are well fit by Bruzual-Charlot solar metallicity, constant-age (4.8 Gyr at $z = 0.9$), variable tau models. Metallicities in these clusters must be at least 0.2 of solar, and a significant amount of dust extinction is unlikely.

We are able to measure significant evolution in the B -band luminosity function over the range $0.1 \leq z \leq 1$. The characteristic luminosity increases by a factor of 3 with increasing redshift over this range. This result is consistent with an analysis of the luminosities of the brightest cluster galaxies in these clusters. The BCGs are typically twice as luminous as their current epoch counterparts.

Subject headings: galaxies: clusters: general – cosmology: observations

1. Introduction

Our understanding of the cosmic history of galaxy clusters is slowly maturing due to an ever growing series of observations including faint spectroscopic data (especially those obtained at the Keck and VLT observatories), deep optical and near-infrared (NIR) imaging from the ground and in space, morphological data from the Hubble Space Telescope (HST), and constraints on the evolution of the intracluster medium (ICM) from ROSAT, ASCA, and XMM. When such observations are applied to complete, objectively derived catalogs of clusters, the constraints placed on cluster formation and evolution scenarios can become quite confined. Cluster evolution is inherently complex both because clusters are not closed systems and because the 3 main mass components (dark matter, ICM, and galaxies) evolve differently. As a consequence, different cluster parameters evolve on different timescales depending on the thermal and dissipative properties of the mass component(s) which most strongly control each cluster parameter.

The properties of clusters at redshifts as low as $z \sim 0.4$ (lookback times of ~ 0.33 the present age of the universe) already exhibit significant departures from their current epoch counterparts. The broad-band color distribution of the early-type galaxy population show significant bluing; the observed trend is consistent with passive stellar evolution and a relatively well synchronized initial starburst epochs occurring at $z > 2.5$ (*e.g.*, Aragón-Salamanca *et al.* 1993; Stanford, Eisenhardt, & Dickinson 1995; Ellis *et al.* 1997). In contrast, the relative abundance and the spectral characteristics of the disk galaxies in clusters appear to have evolved significantly over the last third of a Hubble time (Dressler *et al.* 1997; Poggianti *et al.* 1999). Indeed, the infall and processing of disk galaxies in clusters appears to continue right up to the present day (Adami *et al.* 1998). However, even at $z \sim 0.4$ the properties of cluster galaxies are noticeably different from those in the surrounding field.

At redshifts of $z \gtrsim 0.8$, the study of massive clusters provides particularly important constraints on the physical processes that dominate the formation of their member galaxies (and on cosmological parameters) because the amplitude of evolutionary effects and the differences between competing theories are quite large (*e.g.*, Bower, Kodama, & Terlevich 1998). The observations of clusters at $z \sim 1$ that exist today are limited to a handful of clusters, largely because so few systems are known. While new distant cluster surveys will remedy this lack of targets (*e.g.*, Gladders 2000; Postman *et al.* 2001; Gonzales *et al.* 2001), several intriguing observations of existing systems already suggest that the $z \sim 1$ epoch is one at which clusters and their member galaxies exhibit significant differences from their descendants at $z \lesssim 0.5$. For example, there is evidence that a significant fraction of the early type galaxies in MS-1054 ($z = 0.83$) are merging – something that is not seen in the vast majority of current epoch cluster ellipticals – and which results in a significant increase in the scatter in their color – magnitude relation relative to what is observed at $z < 0.5$ (van Dokkum *et al.* 2000). The fraction of cluster galaxies with evidence for active star formation is also significantly higher at $z > 0.75$ ($\sim 50\%$) than the fraction at the current epoch or even $z \sim 0.5$ (Postman, Lubin, & Oke 1998). At the same time, the global properties of the ICM seem well established even by $z = 0.8$ as there appears to be little evolution observed in

the $L_x - T_x$ relation out to these redshifts (Mushotzky & Scharf 1997; Donahue *et al.* 1998), although the fraction of clusters with asymmetric x-ray gas and asymmetric galaxy surface density distributions increases noticeably (*e.g.*, Lubin & Postman 1996; Gioia *et al.* 1999).

It is quite important, therefore, to conduct statistically complete spectroscopic and photometric surveys of many $z \sim 1$ clusters, covering as broad a range in global cluster properties as possible, in order to understand the breadth of the physics associated with cluster galaxy formation and evolution and, in particular, how the cluster environment modifies the path of galaxy evolution. Focusing solely on one component of the cluster population (*e.g.*, ellipticals) will only reveal part of the story and may even result in a biased interpretation of the timescales for galaxy formation (*e.g.*, van Dokkum & Franx 2001). In 1995, we began an extensive spectroscopic and imaging program to study nine candidate clusters of galaxies at $z \gtrsim 0.7$ (Oke, Postman & Lubin 1998; hereafter Paper I) in an attempt to establish an evolutionary reference sample of clusters analogous to the MORPHs survey performed at $z \sim 0.5$ (Smail *et al.* 1997). Our sole spectroscopic target selection criterion is the galaxy's R -band magnitude. No color selection is applied in order to assure that a broad range of cluster galaxy types are included in the survey. The clusters themselves span a relatively broad range in x-ray luminosity and richness.

In this paper, we present our measurements and interpretations of the kinematic and spectrophotometric properties of the galaxies in the clusters CL1324+3011 ($z = 0.757$), CL1604+4304 ($z = 0.897$), and CL1604+4321 ($z = 0.924$) – the three most massive systems in our survey. CL1604+4321 is of particular interest because its comoving spatial separation from the better known cluster CL1604+4304 is about 15 Mpc and their cosmologically corrected radial velocity separation is 4350 km s^{-1} . Lubin *et al.* (2000) provide extensive observational evidence that suggests CL1604+4304 and CL1604+4321 are indeed two members of a rich supercluster. Some of the spectrophotometric and kinematic results for CL1604+4304 have already been published (Postman, Lubin, & Oke 1998; hereafter Paper II) along with a study of the morphological properties of its galaxy population (Lubin *et al.* 1998; hereafter Paper III). Here we provide both new and improved constraints on the cluster mass estimates, on the evolution of the galaxy luminosity function, and on the spectral characteristics, star formation rates, and stellar population ages of galaxies for all three of the above clusters in this paper. A separate paper (Lubin *et al.* 2001) will present results on the morphological make-up of the cluster galaxies and on the relationship between galaxy morphology and local density in these clusters.

A brief summary of the observations is presented in §2. Our measurements of the cluster masses and mass-to-light ratios are presented in §3 and our constraints on the evolution of the galaxy luminosity function (using both our cluster and field samples) are included in §4. Comparisons between spectral synthesis models and the observed spectrophotometric data are described in §5. A discussion of the characteristics of the brightest cluster galaxies, their evolution, and the “red sequence” is given in §6. Analyses of the star formation rates, stellar population ages, and an improved estimate of the fraction of active galaxies in these clusters are contained in §7 and the correlation of these properties with clustocentric radius

is described in §8. A discussion of the above results along with a summary of our conclusions are given in §9. We adopt $h_{65} \equiv H_o/(65 \text{ km s}^{-1} \text{ Mpc}^{-1}) = 1$, $\Omega_o = 0.2$, and $\Lambda = 0$ throughout this paper.

2. Observations

The photometric and spectroscopic observations of CL1324+3011, CL1604+4304, and CL1604+4321 were conducted using the Low Resolution Imaging Spectrograph at the W. M. Keck Observatory (Oke *et al.* 1995). We provide a brief description of the observations below but refer the reader to Paper I for the full details and to Paper II for the specifics on observations of CL1604+4304.

2.1. Broadband Imaging

Broadband *BVRI* images of CL1324+3011 and CL1604+4321 were acquired during a series of observing runs spread over a 3 year period (March 1994 through August 1997) and were obtained under photometric conditions. We use the SExtractor (Bertin & Arnouts 1996) source detection and classification package to generate object positions, classifications, and aperture photometry from the reduced images. This differs from our work in Paper II where we used the FOCAS (Valdes 1982) package. The aperture photometry from SExtractor is more accurate than that from FOCAS because SExtractor employs pixel masks to exclude light from sources surrounding the object being photometered. We have also reprocessed the image data from CL1604+4304 through the SExtractor package to enable consistent comparisons with the clusters CL1324+3011 and CL1604+4321. The SExtractor detection parameters were set to match the FOCAS parameters described in Paper I. The FWHM of the PSF in the images is $\sim 0.8''$, $\sim 1.0''$, and $\sim 0.9''$ for CL1324+3011, CL1604+4304, and CL1604+4321, respectively. A fixed aperture diameter of $6.0''$ was used to compute the aperture photometry. This diameter corresponds to projected metric radii of $21.7 h_{65}^{-1}$ kpc and $22.9 h_{65}^{-1}$ kpc at $z = 0.76$ and $z = 0.90$, respectively. This aperture choice is consistent with that used for faint galaxy photometry in other intermediate redshift cluster analyses (*e.g.*, Aragón-Salamanca *et al.* 1993, Smail, Ellis & Fitchett 1994, Barger *et al.* 1996).

The number of objects detected and measured is 4952, 3905, and 6322 in CL1324+3011, CL1604+4304, and CL1604+4321, respectively. Not all objects are detected in all four passbands partly because, in some cases, small positional offsets exist between the various filter images whenever the data were obtained on separate observing runs. The number of objects detected refers to only those objects that are detected in *at least* two of the four bands. Spectroscopic target selection, however, is based solely on an object's *R*–band magnitude (see §2.2 below). We also note that all spectroscopically confirmed cluster members are detected in at least 3 of the four passbands so the choice to catalog objects in the above way does not hinder our study of the cluster galaxy populations. Each object is assigned a Keck

identification number (based on its location in a declination-ordered catalog) for convenient referencing. There is a very bright star ($V \approx 10.3$) in the southern part of the CL1604+4321 and objects within $\sim 30''$ of the star are not photometrically analyzed or classified.

All $BVRI$ magnitudes have been converted to absolute AB magnitudes using the relations given in Paper I. Models show that the relation between AB magnitude and $\log \nu$, where ν is the observed effective frequency of each broadband filter, is nearly linear with a small curvature that changes sign when proceeding from hot to cool stellar populations. We have, thus, chosen to characterize the observed broadband energy distributions by the slope, hereafter referred to as the slope b , of a linear least squares fit to the measured AB magnitude as a function of $\log \nu$. The slope b provides a more robust indicator of the overall broadband SED than any individual color measure such as $B - V$, $V - R$, or $R - I$.

The slope b of the cluster and field galaxies are shown as a function of R magnitude in Figure 1 for the CL1324+3011, CL1604+4304, and CL1604+4321 fields. Spectroscopically confirmed cluster members are indicated by the filled symbols. The distributions in slope b are very similar for both cluster and field galaxies; there is only a hint of the red color ridge normally seen in similar plots of clusters at redshifts near 0.5. The lack of a strong red envelope is a consequence of the rest wavelengths of the optical bands used and the relatively young age of the cluster galaxies. A more detailed discussion of this result is provided in §6.2.

2.2. Spectroscopic Observations

Spectra were obtained using several slit masks (7 for CL1324+3011, 6 for CL1604+4321) for galaxies in the range $18 \lesssim R \lesssim 23.5$ (the precise magnitude limits are 23.45 for CL1324+3011 and 23.60 for CL1604+4321). The bright limit was imposed to avoid saturating the detector. The galaxies observed spectroscopically are distributed over a $\sim 2' \times \sim 7'$ region centered on each cluster. Using the procedures described in Paper I, we succeeded in obtaining redshifts for 88% of the objects observed. Table 1 summarizes the yields and Figure 2 shows our redshift success rate as a function of R magnitude. Failure to measure a redshift is mostly due to insufficient signal-to-noise ratio, but occasionally we do encounter good S/N spectra with no identifiable features. Some of the latter spectra may be very low redshift objects without significant absorption or emission features redwards of 5000Å in the rest frame. In CL1324+3011 there is one QSO or AGN, Keck #3933, with a redshift of 1.0750. In CL1604+4321, Keck #1339 is the sole QSO at a redshift of 2.4970.

Tables 2, 3, and 4 provide the key photometric and spectroscopic parameters for all galaxies with measured redshifts for the survey fields centered on CL1324+3011, CL1604+4304, and CL1604+4321. The Keck object identification number is given in column 1 and if the number is preceded by an asterisk then the galaxy is considered to be a member of the cluster (see §3 for details). The brightest cluster galaxy in each case is denoted by a double asterisk. We note that the identification numbers used in Paper II for CL1604+4304 differ

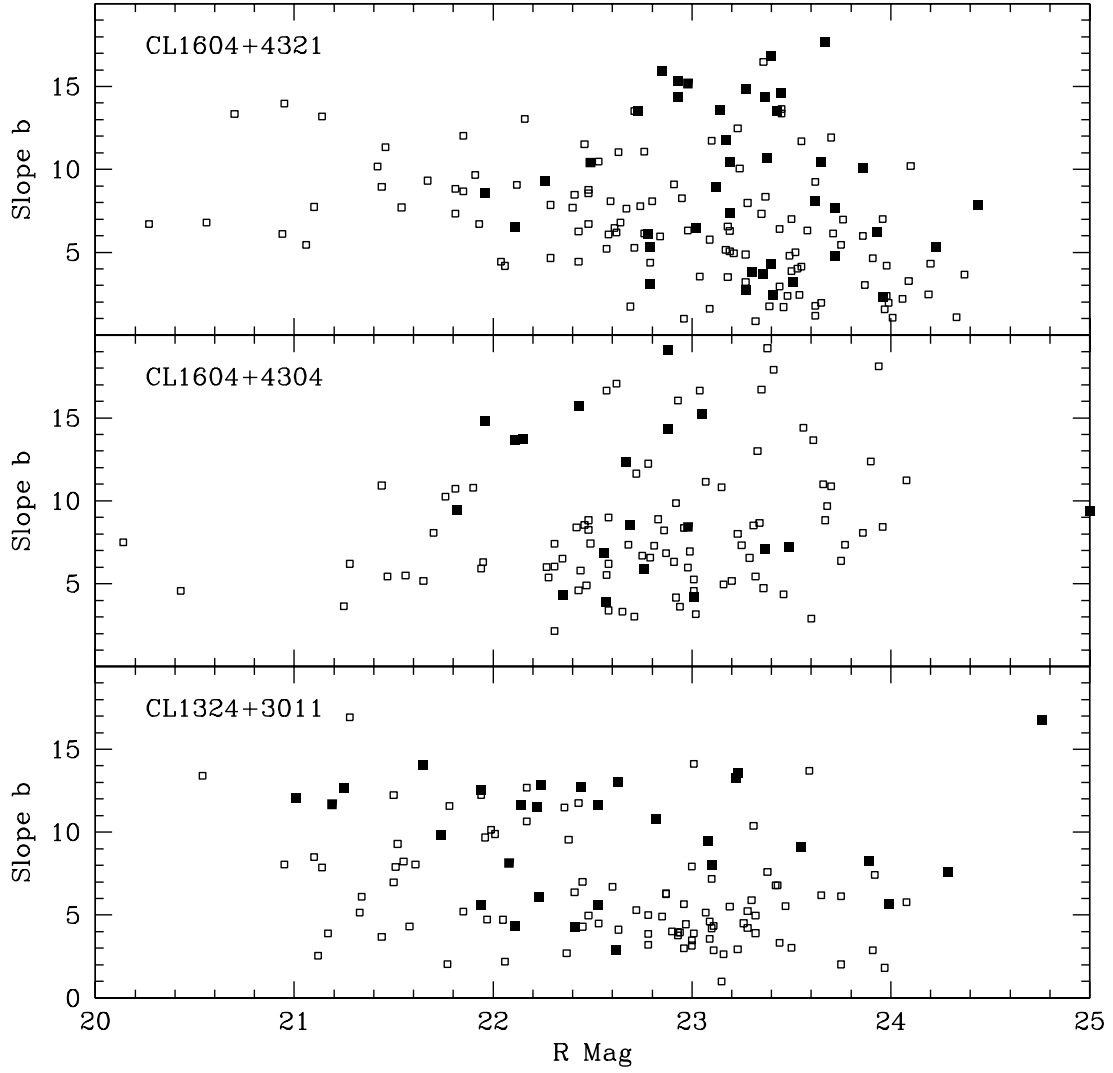


Fig. 1.— The slope of the broadband spectral energy distribution, b , as a function of R magnitude for the fields centered on the clusters CL1324+3011, CL1604+4304, and CL1604+4321. Solid squares are spectroscopically confirmed cluster members while open squares are non-members. The slope b is strongly correlated with the usual broadband color measurements. For example, $(V - R) \approx b/13$.

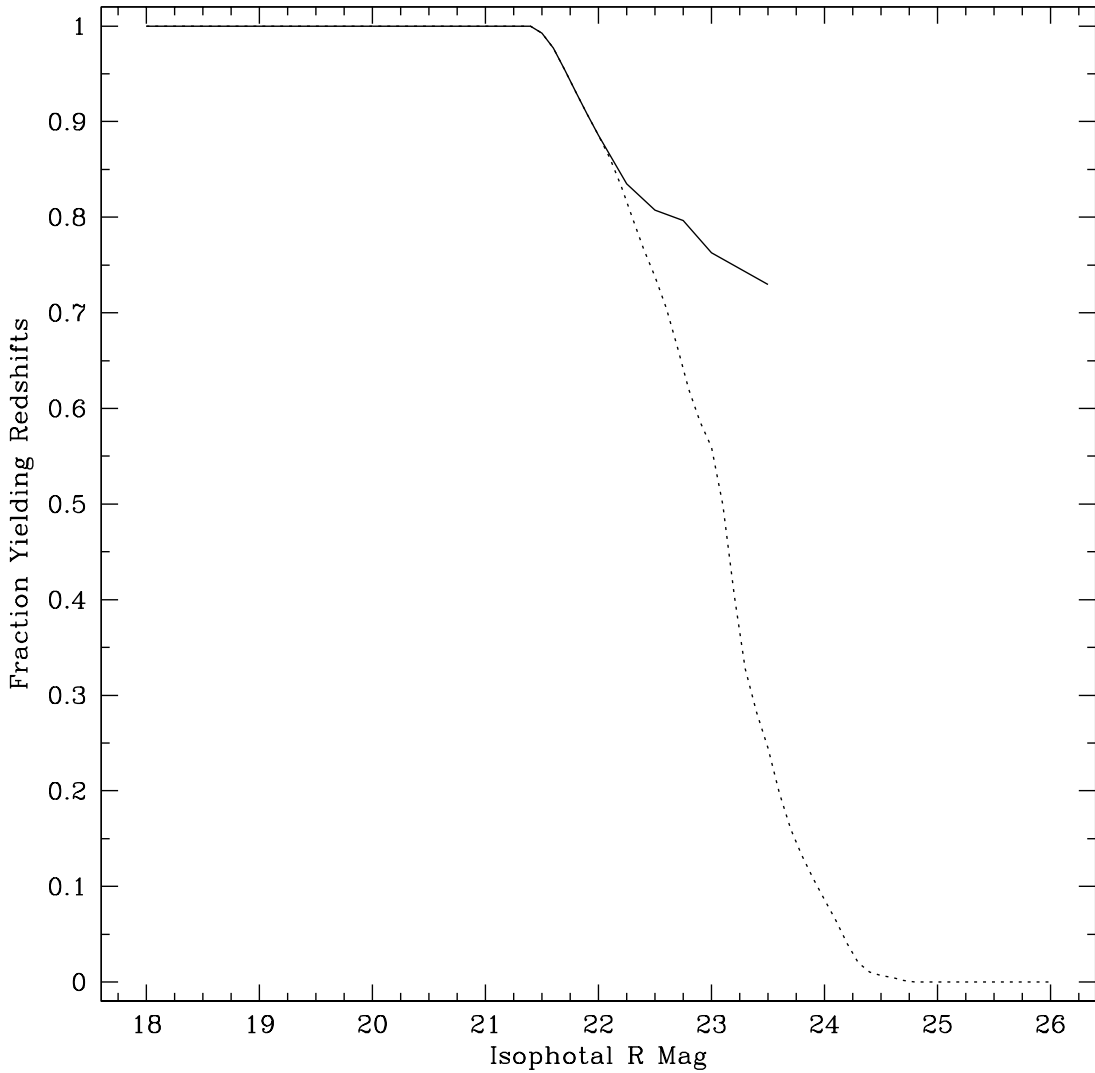


Fig. 2.— The solid curve shows the fraction of spectra for which redshifts were successfully measured as a function of R magnitude. The dashed curve shows the fraction of all galaxies in the field with measured redshifts as a function of R magnitude.

from those in Table 3 because we used different object detection software. The absolute AB magnitudes in our 4 passbands, ABB , ABV , ABR , and ABI , are given in columns 2 through 5. Geocentric redshifts and our measure of the redshift quality (see Paper I) are given in columns 6 and 7. The slope b (defined above in units of AB mag per unit interval of $\log \nu$) is listed in column 8. The contents of the remaining columns are described in subsequent sections.

3. Cluster Mass and M/L Estimates

As in Paper II, we derive cluster masses based on three popular virial theorem mass estimators: the traditional pairwise mass estimator, M_{PW} , the projected mass estimator, M_{PM} (Bahcall & Tremaine 1981; Heisler, Tremaine, & Bahcall 1985), and the ring-wise mass estimator, M_{RW} (Carlberg *et al.* 1996). The mathematical definitions of these estimators are given in equations 2 – 6 in Paper II. Each estimator has its strengths and weaknesses. The M_{PW} estimate does not require one to specify a cluster center. However M_{PM} and M_{RW} , which do require a center to be defined, tend to be much more robust against interlopers. The radial cluster velocity dispersion, a necessary parameter in virial mass estimation, is accurately determined from the redshifts for 22–41 cluster members in each system. Velocity dispersions are computed by first defining a broad redshift range, typically $\Delta z = \pm 0.06$, in which to conduct the calculations. This range is manually chosen to be centered on the approximate redshift of the cluster. We then compute the bi-weight mean and dispersion of the velocity distribution (Beers, Flynn, & Gebhardt 1990) and identify the galaxy with the largest deviation from the mean. Velocity offsets from the mean are taken to be $\Delta v = c(z - \bar{z})/(1 + \bar{z})$ which corrects for cosmological and relativistic effects. In the case of bi-weight statistics, \bar{z} is the median of the distribution. If the galaxy with the largest velocity deviation differs from the bi-weight median by either more than 3σ or by more than 3500 km s $^{-1}$, it is excluded, and the computations are redone. The procedure continues until no further galaxies satisfy the above criteria. The 3500 km s $^{-1}$ limit is based on extensive data available for low z clusters. For example, 95% of the galaxies within the central $4.6h_{65}^{-1}$ Mpc region of the Coma cluster and with $cz \leq 12,000$ km s $^{-1}$ lie within ± 3500 km s $^{-1}$ of the mean Coma redshift. This clipping procedure is conservative and does not impose a Gaussian distribution on the final redshift distribution (see *e.g.*, CL0023+0423 in Paper II).

Figure 3 shows histograms of the velocity offsets relative to the mean cluster redshifts for the three clusters. The derived kinematic parameters, including the mean z , dispersion, and mass estimates, are provided in Table 5. For each cluster, we give the results using all available redshift data (no radius limit), as well as the results for those galaxies within the central 385 and $770h_{65}^{-1}$ kpc regions. The radially limited results are used to derive central mass-to-light (M/L) ratios. The results for CL1604+4304 were originally published in Paper II, but we include them here for convenience. The derived masses within the central $770h_{65}^{-1}$ kpc regions of these 3 clusters are all in excess of $8 \times 10^{14}h_{65}^{-1}$ M $_{\odot}$ (for the M_{PW} estimator) and the projected and ring-wise mass estimators yield central values $\gtrsim 10^{15}h_{65}^{-1}$ M $_{\odot}$. Each of

the clusters has also been detected in X-rays by ROSAT (Castander *et al.* 1994), providing further evidence that these clusters have developed deep potential wells. The 0.1 – 2.4 keV X-ray luminosities are $L_x = (4.80 \pm 1.49) \times 10^{43} h_{65}^{-2}$ erg s $^{-1}$, $L_x = (6.39 \pm 1.37) \times 10^{43} h_{65}^{-2}$ erg s $^{-1}$, and $L_x \leq 4.09 \times 10^{43} h_{65}^{-2}$ erg s $^{-1}$ (3σ upper limit) for CL1324+3011, CL1604+4304, and CL1604+4321, respectively. However, based on the local $L_x - \sigma$ relation (Edge & Stewart 1991), these x-ray luminosities are low for the derived velocity dispersions. Similar trends have been seen in other studies of intermediate redshift ($0.4 < z < 0.7$) clusters (Couch *et al.* 1991; Holden *et al.* 1997; Gioia *et al.* 1999) suggesting that these systems are dynamically young and, consequently, the relationship between the temperature of their x-ray emitting ICM and their total gravitational mass is still undergoing significant evolution.

The central BVR mass-to-light ratios, in solar units, for these clusters are given in Table 6 using the projected mass estimate, M_{PM} , from Table 5. The errors shown include the formal uncertainties in both the mass and luminosity estimates but do not include any systematic error estimates. The cluster luminosities are computed as described in §3.2 of Paper II. The M/L values in Table 6 are based on a non-evolving cluster luminosity function. If we assume that M^* evolves as $M^*(z) \approx M^*(0) - z$ (Lilly *et al.* 1995; see also §4), the M/L ratios increase by about 10%, relative to the non-evolving calculation. The dependence on the evolution of M^* is through the correction applied to the total luminosity for the assumed missing faint end of the cluster luminosity function (see equation 8 in Paper II). Systematic errors in the M/L ratios can be significant, however, because virial equilibrium may not be fully achieved [Small *et al.* (1998) have shown worst case overestimates in the virial mass by a factor of 2 can occur for marginally bound systems] and because the background subtraction is performed statistically, which can be problematic at high redshifts as the light from foreground sources dominates. We minimize this latter effect by confining the luminosity computation to galaxies with apparent magnitudes spanning the range defined by the spectroscopically confirmed members. A correction must still be applied to this luminosity sum, however, to reflect an integration to a common fiducial absolute luminosity, taken to be $-11.15 + 5\log_{10}h_{65}$ in this case.

The central M/L ratios for these three distant clusters are consistent, in mean and scatter, with those seen in their local counterparts (*e.g.*, Girardi *et al.* 2000) covering a range of $100 \lesssim M/L_B < 350h_{65}$, a range inconsistent with an $\Omega_m = 1$ cosmology ($M/L_B = 2355$). However, significant evolution in the M/L ratio on cluster scales is easily masked by the above systematic errors. A more robust measurement of the M/L ratios for these 3 clusters requires substantially more spectroscopic and morphological data than is presently available.

4. Luminosity Function Evolution

The 321 galaxies in these 3 fields with redshifts in the range $0.1 \leq z \leq 1$ allow us to accurately constrain the evolution of the rest AB B -band galaxy luminosity function over the last ~ 0.6 of a Hubble time. The B -band is chosen, as in Paper II, to eliminate or

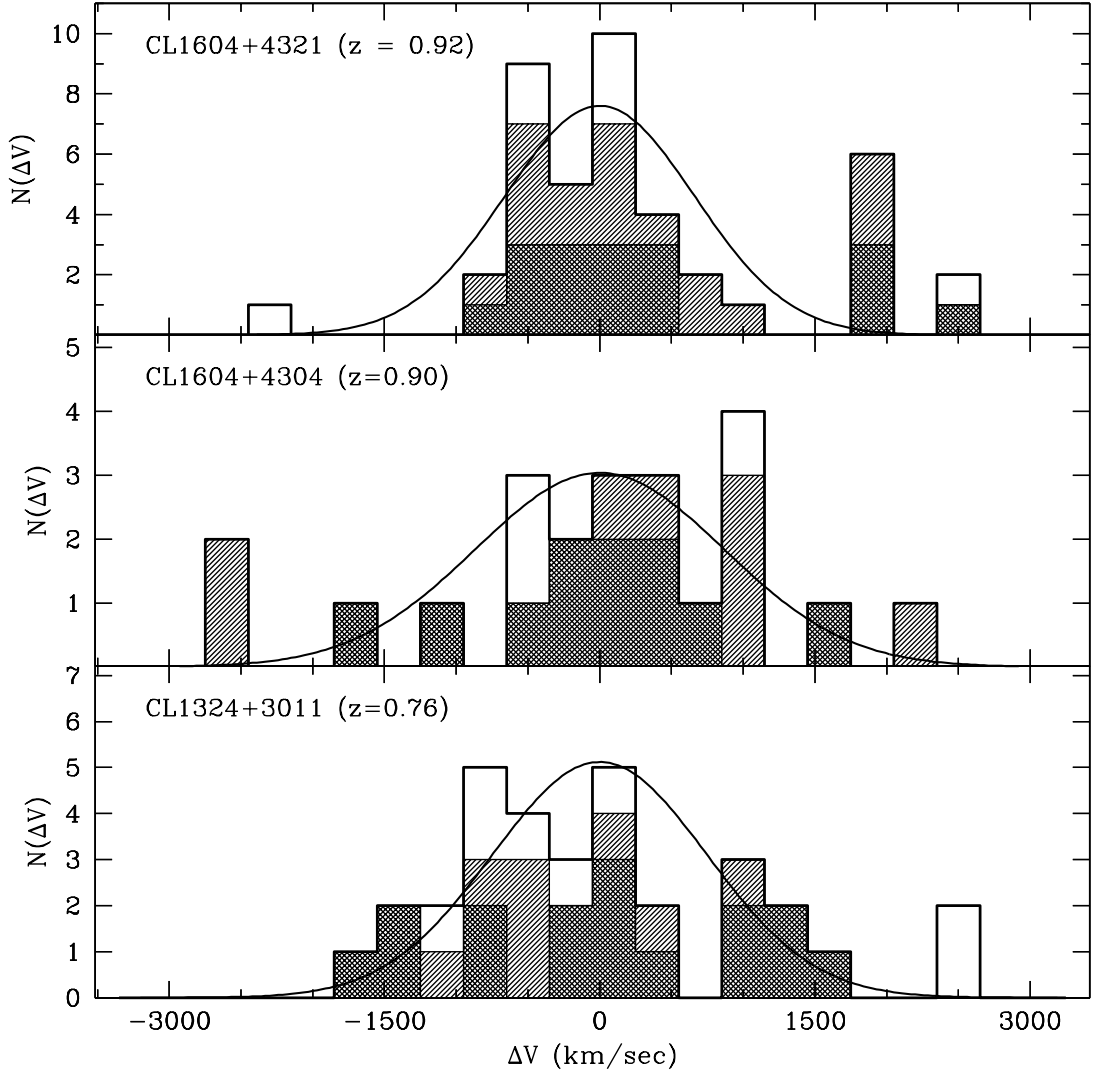


Fig. 3.— Histogram of the relativistically corrected velocity offsets for CL1324+3011, CL1604+4304, and CL1604+4321. Offsets are relative to the mean cluster redshift. Best fit Gaussian distributions are shown for comparison. The darkest histograms include only those galaxies within the central $385h_{65}^{-1}$ kpc. The intermediate shading represents the galaxies within the central $770h_{65}^{-1}$ kpc. The unshaded histograms show the distributions for all available data.

minimize any extrapolation in the calculation of a rest-frame absolute luminosity. We relate apparent and absolute magnitude using the formalism of Equations 6, 9, and 10 in Gunn & Oke (1975). This relation becomes :

$$M_{AB_{\nu(1+z)}} = m_{AB_{\nu}} - 2.5 \log \left[\frac{9.00 \times 10^{20} \mathcal{L}_q^2(z)(1+z)}{H_o^2} \right] \quad (1)$$

where $\mathcal{L}_q(z)$ is given in Equation 9 of Gunn & Oke (1975). The best-fit stellar evolution model to the observed *BVRI* AB magnitudes (see §5) is then used to calculate the absolute magnitude at the rest *B* wavelength from the above expression. The absolute magnitude in this band is hereafter referred to as M_{ABB} . For redshifts of $z < 0.92$ the redshifted *B* filter position is within the observed wavelength range, and an interpolation of the best-fit evolutionary model can be made. Above $z = 0.92$ the rest-frame *B* filter wavelength is above the observed *I* band, and an extrapolation is necessary. This is done using the best-fit evolutionary model and extrapolating to the appropriate frequency. However, 90% of the galaxies in our $0.1 \leq z \leq 1$ sample lie below $z = 0.92$. The uncertainty in the resulting absolute AB can be estimated from the uncertainty in the fit of the observations to the model.

The luminosity function is computed in three redshift bins: $0.1 \leq z < 0.5$, $0.5 \leq z < 0.7$, and $0.7 \leq z \leq 1.0$. Because the latter bin contains the cluster members, we explicitly compute the field and cluster luminosity functions separately for the $0.7 \leq z \leq 1.0$ interval. Each galaxy is weighted by the inverse of V/V_{max} to account for Malmquist bias and by the inverse of the selection function (shown as the dashed curve in Figure 2) to account for the objects for which no redshift was measured. The latter correction assumes that the unmeasured galaxies have the same redshift distribution as a function of apparent *R* magnitude as those that do have measured redshifts. A maximum likelihood method is then used to find the best fit Schechter form luminosity function (Schechter 1976). Because our redshift survey extends only 1.5 magnitudes fainter than the characteristic magnitude, M_{ABB}^* , we constrain the faint end slope of the luminosity function to have a value of $\alpha = -1.15$ (Marzke *et al.* 1998). Figure 4 shows the observations and the best fits for the field galaxy luminosity functions in the three redshift bins. The best-fit M_{ABB}^* values ($h_{65} = 1$) and other relevant details about each redshift bin are provided in Table 7.

The evolution of the *B*-band luminosity function is shown in Figure 5. In this figure we plot the best fit values of M_{ABB}^* as a function of redshift. The horizontal errors are just set by the width of each bin in redshift space. Two simple models for the evolution of the characteristic magnitude are shown. Our data are consistent with an evolution of the form $M^*(z) = M^*(0) - \beta z$ where $1 < \beta < 1.5$. Such evolution is consistent with that reported for blue field galaxies over the range $0.5 < z < 1$ (Lilly *et al.* 1995). The M_{ABB}^* derived for the cluster members is 0.3 mag brighter than that for field galaxies in the range $0.7 \leq z \leq 1.0$. This is expected because the cluster sample includes many luminous early type galaxies which are rarely found in low density environments. The cluster M_{ABB}^* at

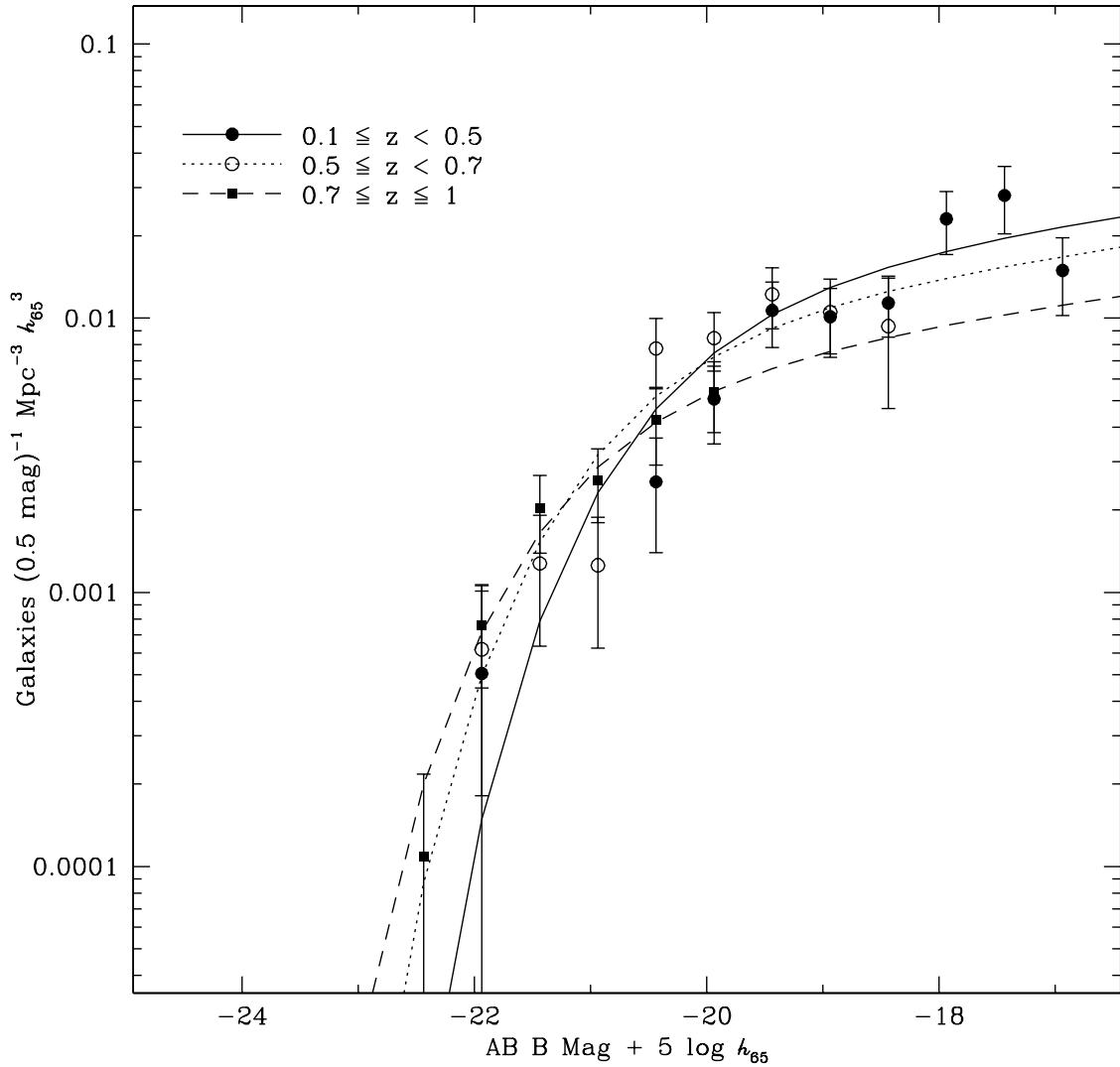


Fig. 4.— The observed data and best fit Schechter luminosity functions for field galaxies in the range $0.1 \leq z \leq 1$. The best fits are constrained to have faint end slopes of -1.15. See text and Table 7 for details.

$z \sim 0.8$ is approximately 0.7 mag brighter than that derived for clusters at $z < 0.2$ (e.g., Colless 1989; Lumsden *et al.* 1997; Valotto *et al.* 1997; Rauzy *et al.* 1998).

5. Spectral Features and Comparisons with Spectral Synthesis Models

5.1. Models

In order to derive constraints on the “ages” of the galaxies in our survey, we use the 1996 stellar evolution models of Bruzual & Charlot (hereafter BC96; see Bruzual & Charlot 1993) because absolute energy distributions can be generated over a broad wavelength range, extending far below the Lyman limit, with a spectral resolution of 20Å, only a factor 2 lower than our observed spectra (see Bruzual & Charlot 1993 for details). The BC96 models can have different metal abundances and we have used those with metallicities of $Z = 0.0200$ (solar) and $Z = 0.0040$ (0.2 solar). The simplest models are ssp models where there is a single instantaneous burst of star formation at time $t = 0$. One can also easily generate models where the star formation rate falls exponentially with time. We have used such models with time constants ranging from 0.2 to 20.0 Gyr. We will refer to these as tau0.2, etc. Unless otherwise noted, models used have solar metallicity. Models with low metal abundance are listed as tau0.6(0040), for example.

Because the models produce absolute energy distributions, it is possible to duplicate almost any measurement that is performed on the observational data. The exception is the measurement of emission line intensities where additional assumptions and calculations, discussed in §5.3, are required.

Any specific model is characterized by the details of the star formation rate (SFR) as a function of the time and the age. A second model parameter is the mean chemical composition. Clearly, there are a large number of possible models, even without varying the chemical composition, and many of them could fit a set of observations for a single galaxy given the measurement uncertainties. We, therefore, consider only two classes of models. For ssp models there is only one parameter and that is the age (in Gyr) after the initial burst of star formation at time $t = 0$. For the tau models there are two parameters, the *e*-folding time for decay of the SFR after $t = 0$ and the age after $t = 0$. As described in Paper II, any model can be used to generate the expected *BVRI* AB magnitudes once the redshift is specified. The most striking characteristic of the models is the change in the slope b , defined in §2.1, as a function of the age. For example, Figure 6 shows the slope b as a function of the logarithm of the model age in Gyr for the ssp model and a series of tau models with different time constants, all computed for a redshift of 0.90.

Over most of the range in b the age derived from the absolute energy distribution depends strongly on the choice of model. At large values of b ($b \geq 15$), the models are very similar and essentially independent of the decay time as long as the decay time constant is less than 0.6 Gyr. We, thus, need to further restrict the range of models that are used. In

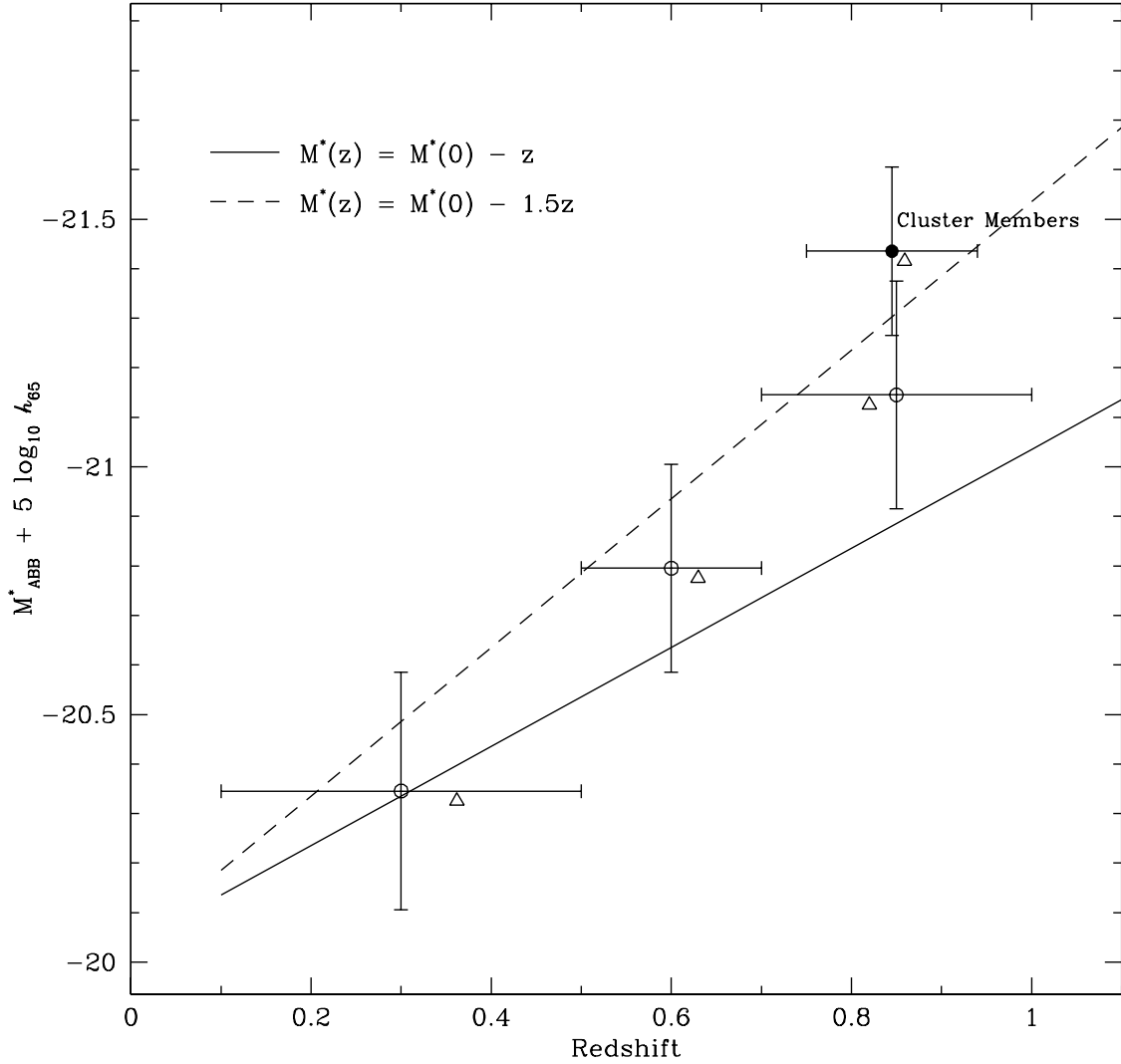


Fig. 5.— The evolution of the luminosity function as traced by the dependence of the characteristic magnitude (for $\alpha = -1.15$) on redshift. Horizontal error bars are set by the width of the redshift bins. Open circles are the results for field galaxies, the filled circle is the result for the cluster galaxies in the range $0.75 \leq z \leq 0.93$. The open triangles show the mean redshift value in each bin. The straight lines show a simple evolutionary model, parameterized as $M^*(z) = M^*(0) - \beta z$, with $\beta = 1$ and $\beta = 1.5$.

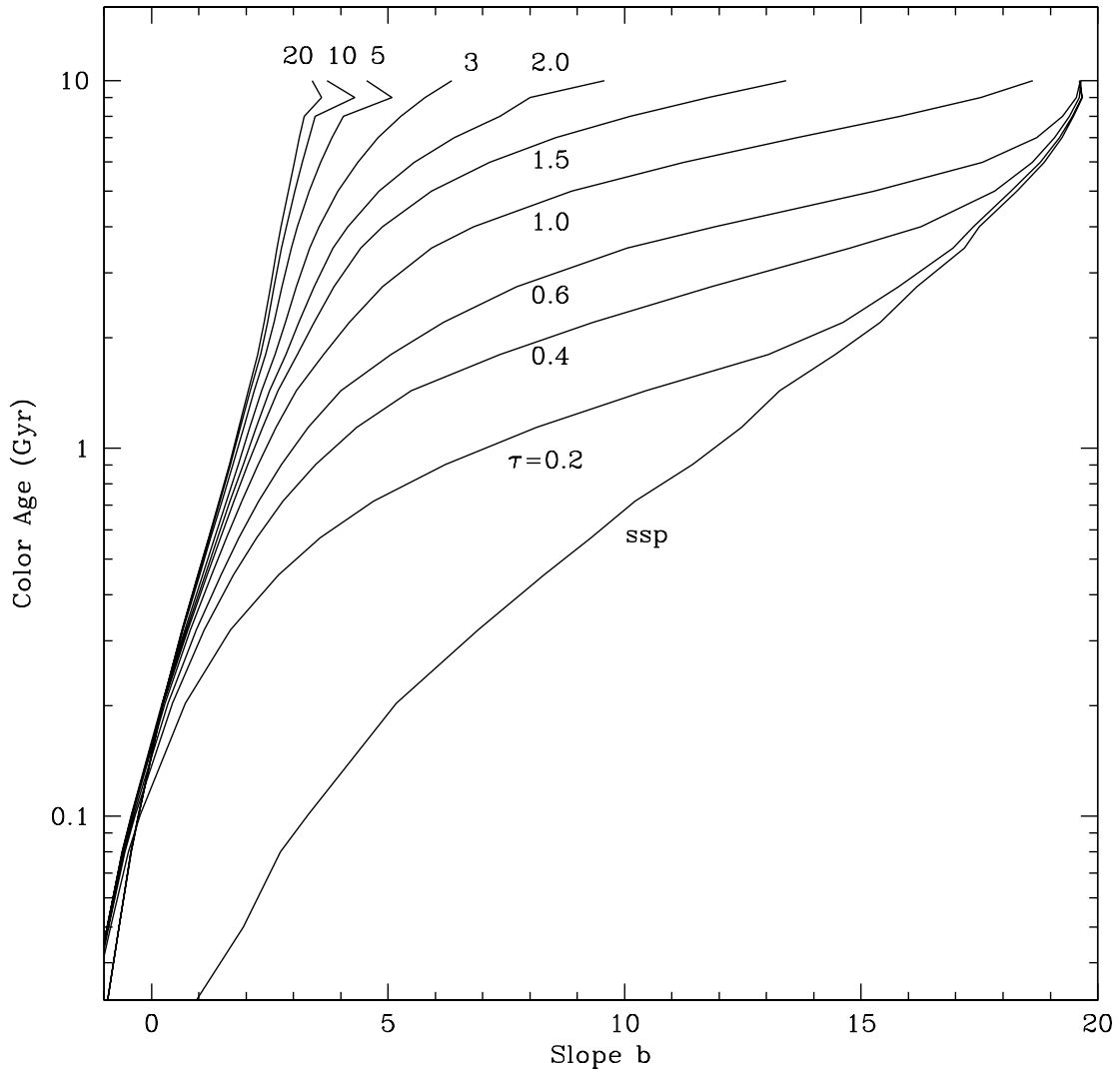


Fig. 6.— The relation between the logarithm of the model age in Gyr and the slope b . The curves from bottom to top represent ssp, $\tau=0.2$, $\tau=0.4$, $\tau=0.6$, $\tau=1.0$, $\tau=1.5$, $\tau=2.0$, $\tau=3.0$, $\tau=5.0$, $\tau=10.0$, and $\tau=20.0$ models.

one extreme scenario, we could specify that the SFR e -folding decay time is constant, say 0.6 Gyr, for all galaxies. In this case, all the fitted models lie along one of the curves in Figure 6. Consequently, the derived ages will vary from 0.1 Gyr to many Gyr because the observed slopes b take on values spanning nearly the total range plotted in Figure 6. This was the basis for the modeling done in Paper II. A somewhat more realistic scenario is to assume that all galaxies (in a given cluster) have the same age and the star formation decay rate is variable. In this case, for clusters at $z=0.9$, the fitted models fall along a horizontal line of the appropriate age in Figure 6. The derived time constants will range from 0.2 Gyr, or less, up to values of 20 Gyr corresponding essentially to a constant star formation rate with time. One should note that there is a region where slope b is small and the ages are greater than 0.1 Gyr where no tau model will fit. Objects observed in this region must have experienced a recent, large burst of star formation the consequences of which are dominating the observed fluxes.

The fits of the model broadband photometry to the observations are done using the maximum likelihood technique described in Paper II. For constant age models, the fitting procedure yields a decay rate and a goodness of fit indicator. Furthermore, the age of all galaxies is assumed to be the time elapsed since the universe was 1.05 Gyr old (for $H_o = 65$, $\Omega_o = 0.2$, $\Lambda_o = 0$ this corresponds to $z = 6.0$). The best fit e -folding times (in Gyr) are listed in column 9 in Tables 2, 3, and 4. If an acceptable fit is not possible for $\tau < 20$ Gyr, the timescale is simply listed as “long”. For consistency with Paper II, where we compared our data only to constant tau models, we also provide (in column 11) the age derived from fitting our broadband BVRI data to the $\tau = 0.6$ family of models (referred to as the “color age” in Paper II).

5.2. Spectral Classification

The features in a galaxy’s spectrum are age-dependent. In particular, the metal lines are weak in young hot objects and rapidly strengthen as the stellar population becomes old. The Balmer lines are fairly weak for young hot objects, rapidly increase to a maximum when A-type stars dominate at ages of about 1 Gyr, and then rapidly become weak thereafter. An important diagnostic of the age and metallicity of a galaxy can thus be gleaned from classification of its spectrum. Our spectral classifications are based on the line strengths of various metal and Balmer absorption features. We do not use equivalent widths as a classification parameter because they tend to have large errors. We do not use emission features in the classification and, thus, differ from the approach used by Dressler et al. (1999) who use the widths of the [OII] and H δ lines as their primary discriminants. We opt to use a *visual* spectral classification scheme because the experienced eye can assess the strengths of all the key features simultaneously and, at the same time, judge the level of noise (including complications such as poor night sky line subtraction). Our spectral classes are defined as follows:

- type “*a*” objects have spectra which are dominated by Balmer lines, lack any g-band absorption, and have a CaII K line strength which is no more than 25% of the strength of the H + He line;
- type “*a+k*” objects have strong Balmer lines, a CaII K line that is approximately 50% of the strength of the H + He line, and a detectable g-band line;
- type “*k+a*” objects have a CaII K line that is equal in strength to H + He, and have a g-band feature that is as strong as H γ , if H γ is not filled with emission;
- type “*k*” objects have a CaII K line is stronger than H + He, have very strong $\lambda 3835$ and g-band features, and exhibit little or no H γ absorption.

Our classes are given in column 10 in Tables 2, 3, and 4. Because the classification scheme above differs from the one used by Dressler et al. (1999), it is important to give a rough translation between the two methods. We achieve this by comparing their sample spectra (Figure 5 of Dressler et al. 1999) with our templates, we find the following correspondence: Dressler “*k*” is equivalent to our “*k*”; Dressler “*k+a*” is between our “*k*” and “*k+a*”; Dressler “*a+k*” corresponds to our “*k+a*”; our “*a+k*” is between Dressler *a+k* and “*e(a)*”; our “*a*” corresponds to the remaining Dressler “*e(a)*”. Note that no classification is provided for galaxies where H γ , H δ , and H ϵ are in emission.

Table 8 provides the specific mean values of equivalent widths and luminosities for each spectral class. Also given in this table, in parentheses, are the 1-sigma statistical errors in the mean values. In Figure 7, we plot histograms of the slope *b* and ABB magnitude for the four spectral classes. The distributions for the confirmed members in all three clusters are shown as shaded histograms. The unshaded histograms show the distributions for field galaxies in the range $0.65 \leq z \leq 1.1$. The mean slope *b* value shows the expected qualitative correlation with the spectral type increasing from $\bar{b} = 5.0$ for class *a* to $\bar{b} = 12.9$ for class *k*. In other words, the older, more metal rich galaxies tend to be, on average, redder. The *k* type galaxies also tend to be significantly brighter (by 0.7 - 1 mag) than *a* type galaxies, a trend most likely attributed to the dominance of massive elliptical galaxies in the *k* spectral class. These results are consistent with those reported by Poggianti *et al.* (1999).

5.3. Emission Line Equivalent Widths and Intensities

Emission line equivalent widths are measured as described in Paper II. As our sample is dominated by galaxies at high redshift, the spectral region containing the [OII] line is nearly always observed. The H β and [OIII] regions are also observed for the majority of objects with $z \lesssim 0.95$, but at values of z above 0.8 the signal is low and the night-sky emission bands are very strong. In a few low redshift galaxies the H α region is observed. Equivalent widths in Angstroms, corrected to the rest-frame, have been measured for [OII] $\lambda 3727$, H β , and [OIII] $\lambda 5007$. These emission lines are often strong and are well isolated

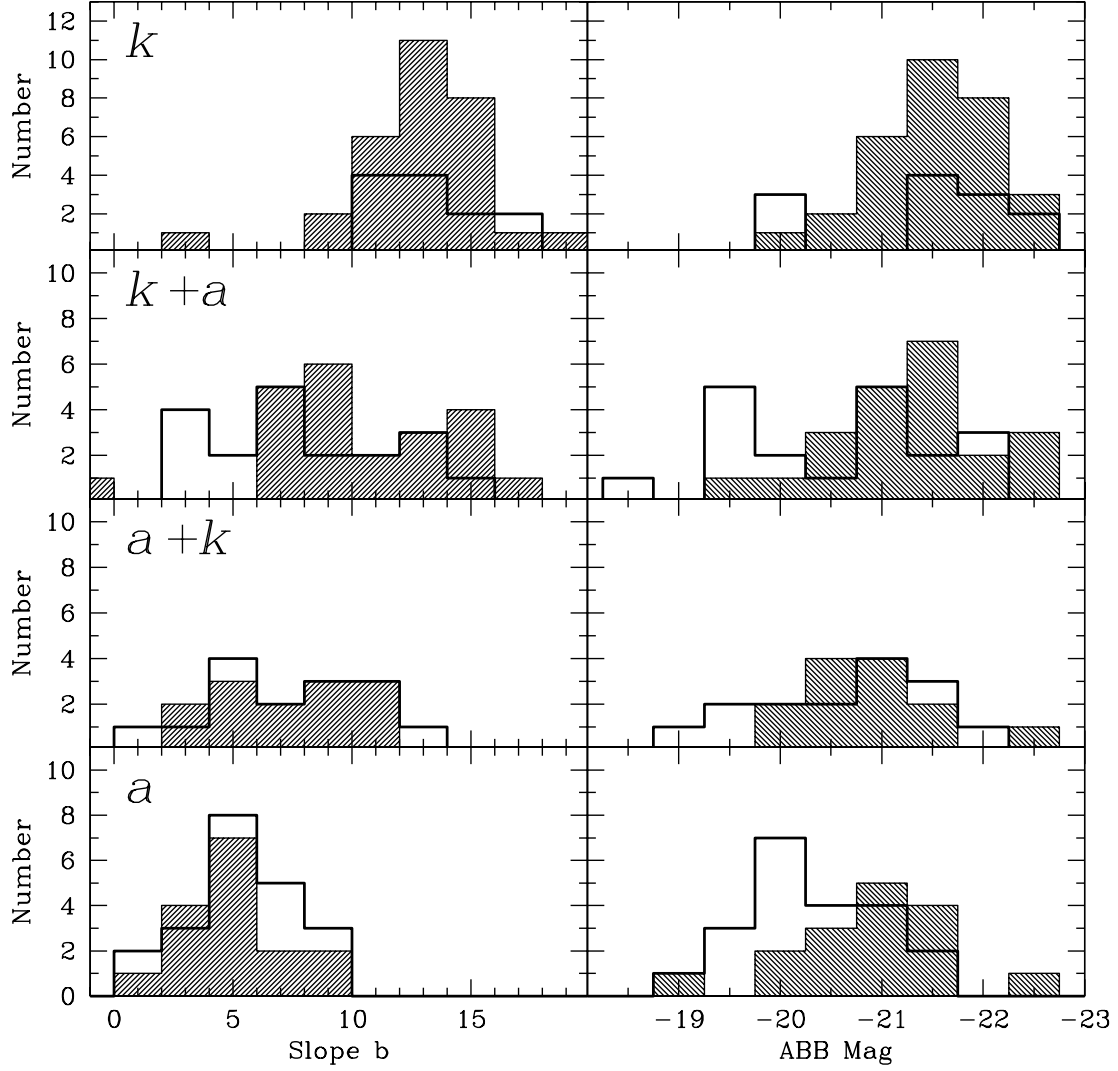


Fig. 7.— The slope b and ABB magnitude histograms as functions of the spectral classification a , $a+k$, $k+a$, and k are shown. The distributions for spectroscopically confirmed cluster members are shown as shaded histograms. The histograms for field galaxies in the range $0.65 \leq z \leq 1.1$ are unshaded.

from other spectral features. Emission line equivalent widths are given as negative values (positive values are used for absorption features). The equivalent width of $H\beta$ can be either negative or positive since the line lies on top of the possible absorption feature. The typical errors in the equivalent widths are estimated from the differences between rest equivalent widths derived from two independent and comparable spectra of the same object. For the current sample, we have a total of 54 such overlap observations with $0.5 \lesssim z \lesssim 1.0$. The comparisons suggest errors of $\sim 5\text{\AA}$ for the [OII] line and $6 - 8\text{\AA}$ for the $H\beta$ and [OIII] $\lambda 5007$ lines. The rest equivalent widths in Angstroms of [OII], $H\beta$, and [OIII] are given in columns 12 through 14 in Tables 2, 3, and 4. No corrections for underlying absorption have been applied to the $H\beta$ equivalent widths listed in the tables.

Emission line intensities are calculated by measuring the observed flux of the continuum at the line and converting the equivalent widths to intensities. For the $H\beta$ line, this conversion is

$$\log(I(H\beta)) = \log(EW(H\beta)) - 0.4AB(4861)_{absol} + 31.74 \quad (2)$$

where $AB(4861)_{absol}$ is the observed AB magnitude of the continuum measured at the redshifted position of $H\beta$, converted to an absolute magnitude using the distance modulus. The intensity $I(H\beta)$ is in units of erg s^{-1} . Similar equations apply to the [OII] and [OIII] lines: the zeropoints are 31.97 for the [OII] line and 31.72 for the [OIII] line. The continuum is interpolated using the broadband AB magnitudes and the fitted models. In these intensity calculations a correction for the equivalent width of the absorption line underlying $H\beta$ has been applied based on the spectral synthesis model being compared to the data. The correction is typically 3 to 8\AA .

We validate our line intensity measurements by comparing line ratios to previously published work. Specifically, we use the best spectra in the appropriate redshift range to derive a mean observed intensity ratio of [OII] to $H\beta$ and [OIII] to $H\beta$. Averaging the logarithms of the observed intensity ratios we find $I([OII])/I(H\beta) = 2.19$ and $I([OIII])/I(H\beta) = 1.81$. Because the redshifts are high, and the galaxies are small on the sky, these represent averages over the whole galaxy. Kennicutt (1992) has measured these ratios in nearby, mostly late-type galaxies using large apertures and small telescopes. His better data give ratios of 2.40 and 1.48, respectively. These lines have been measured by van Zee *et al.* (1998) in many HII regions over the whole surfaces of a variety of spiral galaxies. After removing their corrections for reddening, their average ratios are 2.14 and 1.09, respectively. The intrinsic scatter is about 50% for $I([OII])/I(H\beta)$ and about a factor 2 for $I([OIII])/I(H\beta)$. Our results agree quite well, given the scatter, with the results of Kennicutt and Van Zee *et al.* although our average [OIII] to $H\beta$ ratio is higher than that in those two studies.

5.4. Metal-Line Equivalent Widths

Although we have measured eight absorption lines in the galaxy spectra, they are not all equally useful. Among the metal lines, the $\lambda 3835$ feature is in a spectral region where any continuum choice is rather arbitrary. The feature is strong in the redder objects but it is superposed on the Balmer H9 line, which will be relevant for bluer galaxies. The CaII H line is superposed on He. The g-band is close to H γ but sufficiently separated from it to be measurable; it is usually sufficiently far in the red to be in a rather noisy spectral range. Of the available Balmer lines, H γ is always suspect since it may be partially or completely filled with emission. H δ should be reliable. H8 is in a crowded spectral region where a continuum is very hard to estimate.

The rest equivalent widths of the $\lambda 3835$ feature, CaII K and the g-band are plotted against the continuum slope b in Figure 8 for cluster members. In this figure, and in subsequent similar ones, cluster members in the three clusters CL1324+3011, CL1604+4304, and CL1604+4321 are indicated by open circles, filled circles, and filled squares, respectively. The errors in the highest S/N equivalent width measurements of the $\lambda 3835$ line, the CaII K line, H δ , and the g-band are, respectively, 1.8, 1.6, 3.0, and 2.3 \AA . The mean equivalent widths as a function of slope b for the sub-sample of red and blue galaxies with the best spectra are given in Table 8.

To compare the absorption-line data with the models it is desirable to use models with approximately the same spectral resolution as the observations. The BC96 model spectra have a resolution or binning size of 20 \AA which is twice as large as the spectral resolution of our observations making direct comparisons with the data difficult. The 1993 Bruzual & Charlot (BC93) models, on the other hand, have a resolution of 10 \AA and are, thus, ideal for comparisons with observational data. Furthermore, a comparison of the Bruzual & Charlot 1993 and 1996 models with the bandpasses optimized for the 1996 models shows that the absorption equivalent widths are larger for the 1996 models by factors that vary from 1.27 to 1.69 depending on the line being measured. That the factor varies from line to line strongly suggests that the mismatched spectral resolution is indeed at least part of the source of the discrepancy. Further evidence in support of this explanation comes from the excellent agreement between the equivalent widths obtained from a very high S/N spectrum of NGC 4889 in the Coma cluster⁴ and the BC93 solar metallicity models. We therefore make comparisons of observed and measured line equivalent widths using the BC93 models.

The line strengths from the BC93 solar metallicity tau0.3, tau0.6, and tau1.0 models, all with an age of 4.8 Gyr which is close to that expected for cluster galaxies at $z \sim 0.9$, are shown in Figure 8 as the solid curves. The figure demonstrates that the BC93 equivalent widths are in very good agreement with the corresponding values for our distant cluster galaxies.

⁴The NGC 4889 spectrum was obtained with the Double Spectrograph on the Hale 5m telescope at Palomar Observatory.

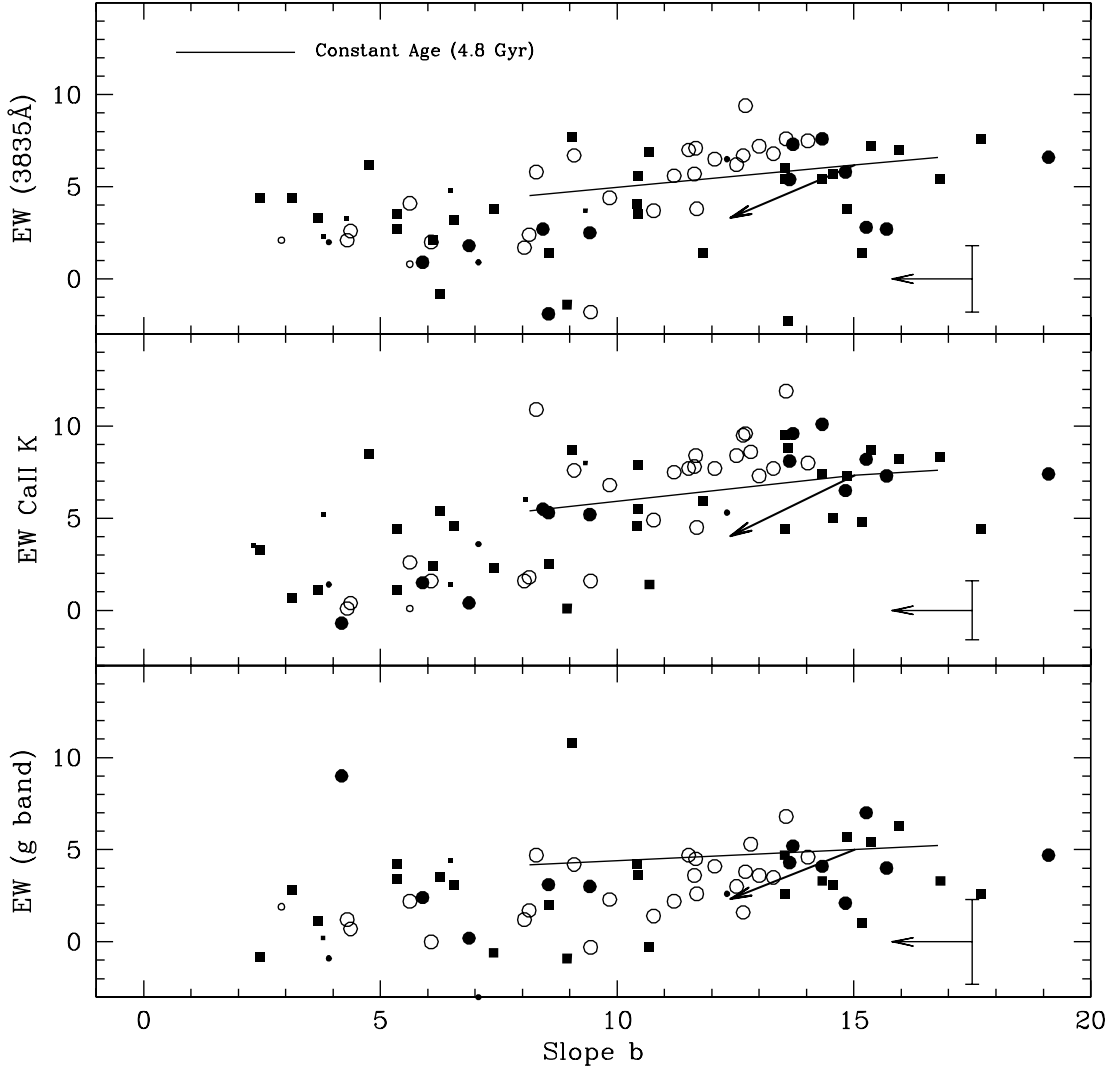


Fig. 8.— The relation between the rest equivalent width (in Angstroms) of the $\lambda 3835$, CaII K, and g-band spectral features and the slope b for confirmed cluster members. The predictions from the Bruzual & Charlot (1993) solar metallicity model with a constant age (4.8 Gyr at $z = 0.90$) are shown by the solid line. The open circles, filled circles, and filled squares display the observations (uncorrected for reddening) for CL1324+3011, CL1604+4304, and CL1604+4321, respectively. The larger symbols represent results based on very high S/N spectra. A typical observation error bar is shown. The observations are shown uncorrected for reddening. The arrow on the error bar shows how the data would shift if corrected for a reddening of $E(B-V) = 0.2$ mag. The diagonal arrow on the model curve shows how the model shifts when the metallicity is reduced to 0.2 solar.

5.5. The Balmer Jump and the 4000Å Break

The conventional 4000Å discontinuity measure, D , is not particularly useful for the analysis of young stellar systems (like those in distant, late-type galaxies) because it does not enable one to discriminate between spectra that are dominated by metal-line absorption from cool stars and by spectra dominated by the high Balmer lines and the Balmer jump in A-type stars. Furthermore, the measurement D does not remove the overall color of the object that depends on both the spectral energy distribution and on the wavelength response of the detector (because our spectra are not flux calibrated). We prefer instead to use the J parameter (first proposed in Paper II). For the present analysis, we define two slightly modified jump parameters, J_l and J_u . Continuum points are computed by first establishing the mean slope of the spectrum in the rest-frame spectral range 4050–4650Å, which is usually much better exposed than the region below 3700Å. Points near H δ (4075Å to 4125Å) and the g-band and H γ (4280Å to 4350Å) are excluded from the calculations. The level of this continuum is normalized to match the mean AB flux in the range 4000 to 4280Å. This normalized continuum level and the measured slope are then used to extrapolate a continuum in the 3750 to 3980Å and 3400 to 3700Å regions. Figure 9 provides a schematic description of the jump definitions.

The jump J_l is defined as the difference of the average flux (expressed in AB magnitudes) measured from 3400 to 3700Å and the defined continuum at the central wavelength of this band (*i.e.*, 3550Å). The jump J_u is defined as the difference of the average flux (again in AB magnitudes) in the range 3750 to 3980Å and the defined continuum at the central wavelength of 3865Å. J_u is very similar to the conventional jump D except that the continuum slope has been removed. It essentially measures the strength of the discontinuity at 4000Å caused by metal and late Balmer series absorption lines. J_l measures the Balmer jump produced by hydrogen absorption plus any metal-line blanketing in the 3400 to 3700Å region. Since both J_l and J_u depend on an extrapolation of the continuum that is defined above 4000Å, they are subject to systematic errors caused by loss of light due to refraction and absolute calibration errors in the blue relative to the red spectral region. This effect should be small for J_u but can be large for J_l . Subject to these systematic errors, the ratio of J_u to J_l is a measure of the relative importance of the Balmer jump and the 4000Å break. If the 4000Å break is large, both J_u and J_l will be close to unity. If the Balmer Jump dominates, J_u will be less than half of J_l . The measured values of J_u and J_l are given in columns 15 and 16 in Tables 2, 3, and 4. Errors have been estimated in the same manner as those for the equivalent widths. The typical errors in J_u and J_l are 0.10 mag and 0.13 mag, respectively.

The observed values of J_u and J_l are plotted against the observed slope b for members of the three clusters in Figure 10. Representative error bars are shown. The large open diamonds show the mean jump values in four slope b bins for the highest quality spectra only. These mean values are consistent with the full data distribution, indicating that no serious systematic errors are introduced into the jump estimates at lower signal-to-noise levels.

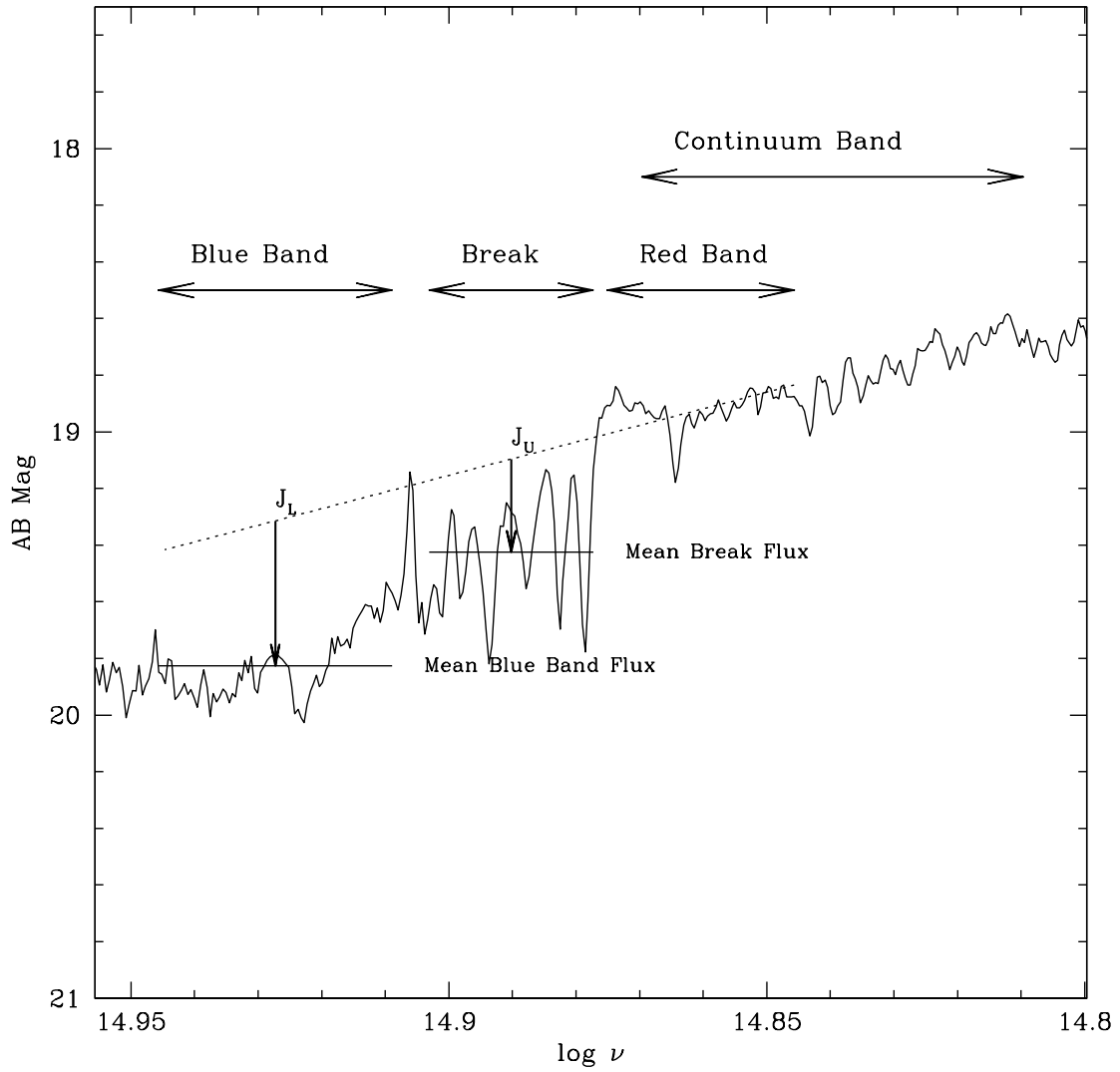


Fig. 9.— A visualization of the definitions of the J_l and J_u jump amplitudes. The dashed line is the extrapolation of the continuum level, normalized to the mean red band flux. The jump amplitudes are measured with respect to this extrapolation.

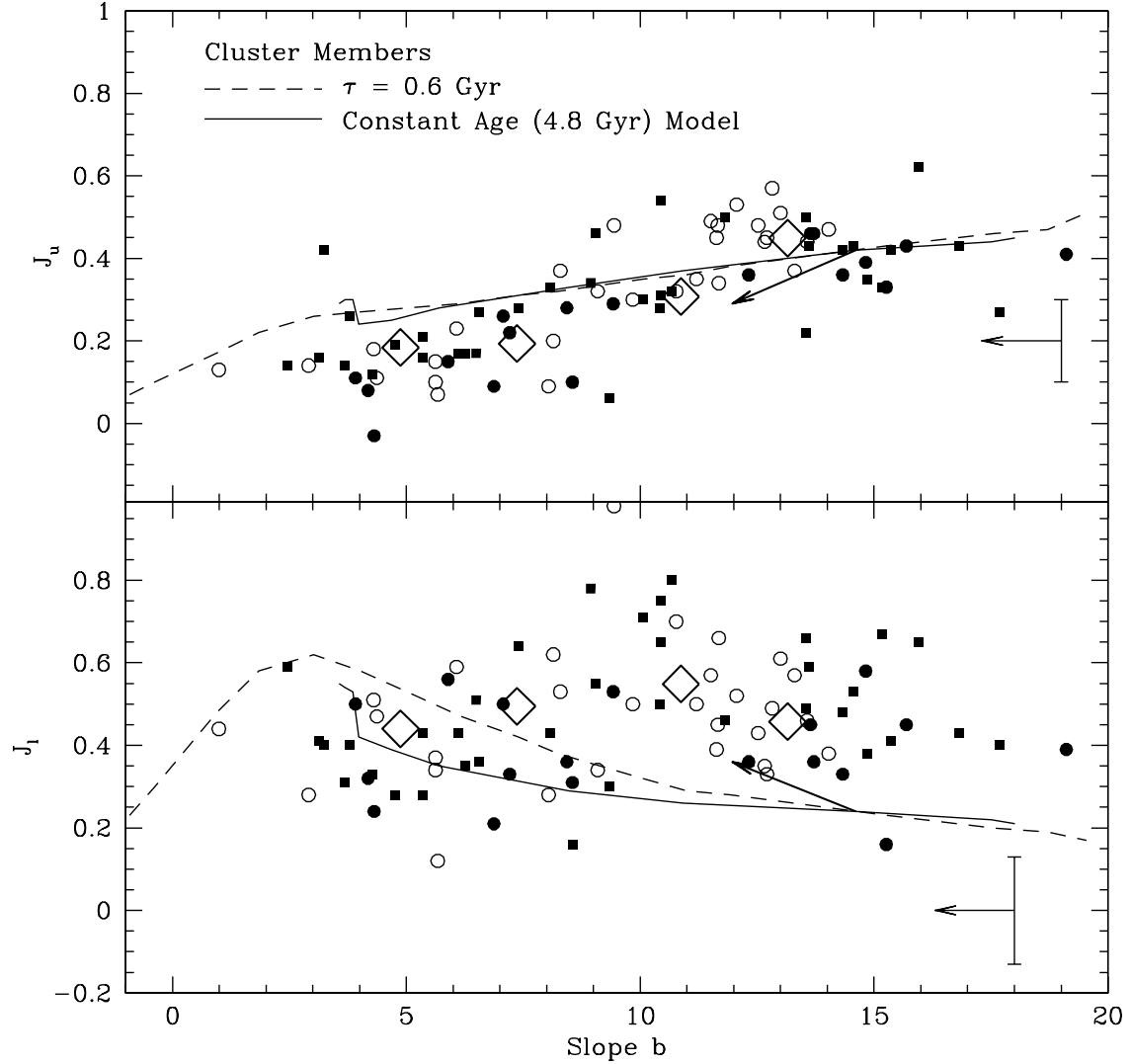


Fig. 10.— The upper and lower jumps (J_u and J_l) in AB magnitudes as functions of the slope b for galaxies in the clusters are shown in the upper and lower plots, respectively. The symbols and arrows are as defined in Figure 8. Typical error bars are shown. Large open diamonds show mean values in four bins for the highest quality spectra. The broken curves are for tau0.6 solar metallicity BC96 models of various ages with redshift $z = 0.9$. The solid curves are for constant age models. A typical observation error bar is shown. The observations are shown uncorrected for reddening. The arrow on the error bar shows how the data would shift if corrected for a reddening of $E(B-V) = 0.2$ mag. The diagonal arrow on the model curve shows how the model shifts when the metallicity is reduced to 0.2 solar.

The solid curve shows the jump values predicted by our constant age scenario models. The dashed curve shows the predictions from a solar metallicity tau0.6 model. The small discontinuity in the constant age model predictions at small slope b values appears to be caused by some difference in the tau5.0, tau10.0, and tau20.0 models or in our interpretation of the models.

The solar metallicity models do a reasonable job of reproducing the observed correlation between J_u and the slope b . There is no significant observed correlation between J_l and the slope b . This is, in part, due to the fact that J_l is affected both by the Balmer jump and the 4000Å break which tend to evolve in a manner which minimizes the change in J_l . Furthermore, the absolute values of J_l are subject to large systematic errors (more than J_u), and the difference between the observations and models is not significant when these errors are taken into account.

5.6. Metallicity and Reddening

To obtain rough constraints on the metallicities of the galaxies in our survey, we must rely on comparisons with the BC96 models as the BC93 models do not include non-solar models. In the following, we therefore use the measured BC96 equivalent widths scaled to correct for the spectral resolution difference between the BC96 models and LRIS data. The vectors drawn in Figures 8 and 10 show how the reddest models shift when the metallicity is changed from solar to 0.2 solar. The shift that is shown is typical when the slope b is greater than 6. At small b , the shift is smaller because the metal lines have diminished in strength. The observed CaII K and the $\lambda 3835$ features show excellent consistency with the solar metallicity models. The g-band measurements would be fitted better with slightly sub-solar metallicity models. The uncertainties, however, are too large to be definitive. The J_u data suggest that a metallicity slightly less than solar would fit the data best. For J_l the fits of the models to the observations are all poor. This may indicate that a substantial amount of the blue light from the galaxy is being lost at the slit.

Corrections for reddening will change the slope b but not the jumps or equivalent widths. The horizontal arrows on the representative error bars in the above figures show how the data points would shift if a 0.2 mag de-reddening correction were applied. A reddening of 0.2 mag in $B - V$ corresponds to a change in slope b of 1.7. Such a reddening correction would not significantly alter the fits to the models. A much larger reddening correction, however, would make the fits of the equivalent widths unacceptable.

6. Cluster Properties

6.1. Brightest Cluster Galaxies

The absolute AB magnitudes of the galaxies in the rest B band, M_{ABB} , have been calculated as described in §2.2.2 of Paper II and are listed in column 18 of Tables 2, 3, and 4. Figure 11 shows M_{ABB} plotted against the redshift z . The lower boundary of points is a consequence of the survey magnitude limit. The upper boundary at lower values of z is strongly influenced by the small volume sampled at low redshifts.

The M_{ABB} magnitudes predicted by the tau0.2, tau0.6, and tau1.0 models are listed in Table 9 as a function of z and are plotted in Figure 11. (The results for ssp and tau0.2 models are almost identical since there is virtually no star formation and evolution is proceeding slowly.) The constant age scenario is assumed, that is, star formation commenced 1.05 Gyr after the universe began. The curves are normalized to match the $z \leq 0.05$ brightest cluster galaxy (BCG) sample of Postman & Lauer (1995) which, after correcting their results to conform to $H_o = 65$ and a metric radius of $22.3h_{65}^{-1}$ kpc (to match our aperture photometry at $0.76 \lesssim z \lesssim 0.92$), and adopting a mean α parameter value of 0.50, gives $M_{ABB,BCG} = -21.81$ at $z \leq 0.05$.

Changing the star-formation-rate decay time from 0.2 to 1.0 Gyr yields a significant change in the BCG luminosity, ~ 0.5 mag by $z = 1$, since star formation becomes increasingly important. The median value of tau for our constant age models is 1.0 Gyr. For the same models, the result of changing from $H_o = 65$ to $H_o = 80$ is shown in Table 9. This change makes a relatively small difference, even at high z ($\lesssim 0.2$ mag by $z = 1.5$). The BCG in CL1324+3011, Keck #2151, has $M_{ABB} = -22.44$. The best fit constant age scenario model gives a decay time of $\tau = 0.9$ Gyr and predicts $M_{ABB} = -22.84$. The BCG in CL1604+4304, Keck #1888, has $M_{ABB} = -22.51$. The best fit model gives $\tau = 0.6$ Gyr and predicts $M_{ABB} = -22.86$. The BCG in CL1604+4321, Keck #1292, has $M_{ABB} = -22.52$. The best fit model gives $\tau = 0.9$ Gyr and predicts $M_{ABB} = -23.06$. On average, the models predict a BCG magnitude that is ~ 0.4 mag brighter than observed.

6.2. The “Red Envelope”

One of the striking features of the galaxies in our three samples is the large spread in the color of the cluster members, as measured by the slope b . This is dramatically demonstrated in Figure 12. As in Figure 1, there is almost no sign of the red color ridge that is often seen in clusters at $z = 0.5$ (*e.g.*, Oke, Gunn, & Hoessel 1996; Stanford, Eisenhardt, & Dickinson 1998, hereafter SED98) although there are still quite a number of red galaxies in the samples. The visibility of the red ridge at $z = 0.9$ is a bit more prominent when a near-infrared color is used, as the CM diagrams of SED98 demonstrate. All of the objects in the $z = 0.9$ clusters with slope b greater than 13 to 14 correspond to the central concentration of red galaxies. In CL1324+3011 ($z = 0.76$) the galaxies populating the red ridge have b greater than 11. The broad color distribution of cluster galaxies at $z \gtrsim 0.8$ is compatible with the evolution predicted from our family of tau models. This is demonstrated by the curves in

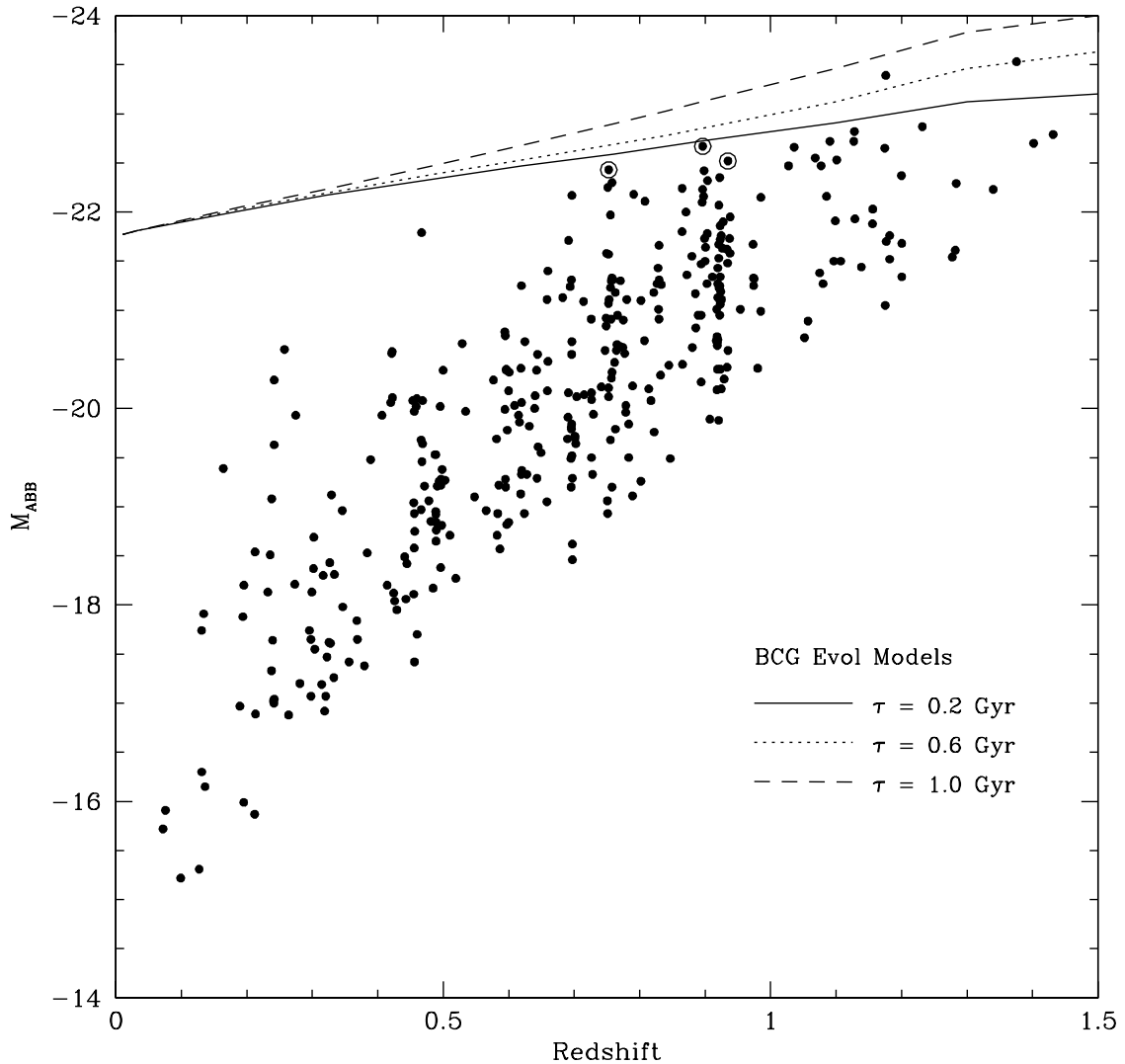


Fig. 11.— The absolute AB magnitude in the rest frame B band as a function of redshift for all galaxies with measured redshifts. The data for the brightest cluster galaxy for each cluster is highlighted with a large open circle. The redshift evolution of the BCG magnitude for the $\tau_{0.2}$, $\tau_{0.6}$, and $\tau_{1.0}$ models are also shown.

Figure 12 which show how the b slope of galaxies evolves with redshift. The nine curves from bottom to top correspond to the BC96 tau20.0, tau10.0, tau5.0, tau2.0, tau1.5, tau1.0, tau0.8, tau0.6, and tau0.2 families of models. Specifically, the model spectra are allowed to age by times that are calculated assuming $H_o = 65$, $\Omega_o = 0.2$, and by assuming that star formation commenced 1.05 Gyr after the universe began. As can be seen, all of the objects at $z=0.9$ with values of b between 7 and 19 have collapsed into a much narrower range from 11 to 12.5 by $z=0.5$, corresponding to a range in $V - R$ or $R - I$ of 0.1 mag. The red ridge is, thus, predicted to contain a much larger fraction of the galaxies in a cluster at $z = 0.5$ than at $z = 0.9$, making the envelope much more prominent at the lower redshifts. This is clearly what is seen in our the results and those from SED98. The bluest objects at $z=0.9$ remain very blue by $z=0.5$, however. The set of models shown in Figure 12 encompass nearly all the galaxies seen at all redshifts. There are a few objects that are even bluer than our most extreme model. These are presumably objects where there has been a recent very strong burst of star formation.

7. Emission Line Intensities and Star Formation Rates

7.1. Fraction of Active Galaxies

In Paper II we demonstrated the strong evolution in the fraction of active galaxies, defined to be those galaxies with [OII] rest equivalent widths greater than 15Å, in the field and in clusters at $z > 0.7$ relative to what is seen at the present epoch. We now provide an improved constraint by including the results from CL1324+3011 and CL1604+4321. In total there are 345 galaxies with redshifts and 25 additional galaxies without redshifts but that have sufficiently high S/N spectra that we can be fairly sure there are no emission lines. Ten objects with low redshifts have strong $H\beta$ and [OIII] but [OII] lies bluewards of the observed spectral range. For field galaxies with $0.40 < z \leq 0.85$, 65% are active. For field galaxies with $z > 0.85$, the fraction is 79%. For roughly the same range in redshift, Hammer *et al.* (1997) find quite comparable values of 65% and 90%. Within the central $1.5 h_{65}^{-1}$ Mpc regions of our three distant clusters, the fraction of active galaxies is 45%. This is substantially higher than the 10 to 20% active galaxy component seen in the centers of $0.2 < z < 0.55$ clusters (Balogh *et al.* 1997) but significantly lower than the active fraction in the surrounding field.

We must examine whether or not our R -band selection criterion biases our estimate of the active galaxy fraction. The [OII] line redshifts into the R passband at $z \approx 0.53$ and redshifts out of the R passband at $z \approx 1.15$. Hence, one could imagine that selecting targets for spectroscopy based solely on the object's R -band magnitude might potentially bias the sample in favor of objects with strong [OII] emission near the survey magnitude limit and, consequently, cause the active fractions to be overestimated. Our selection criterion, however, does not appear to have a significant effect. We demonstrate this in two ways. First, the lower plot in Figure 13 shows the [OII] equivalent width as a function of the galaxy R -band

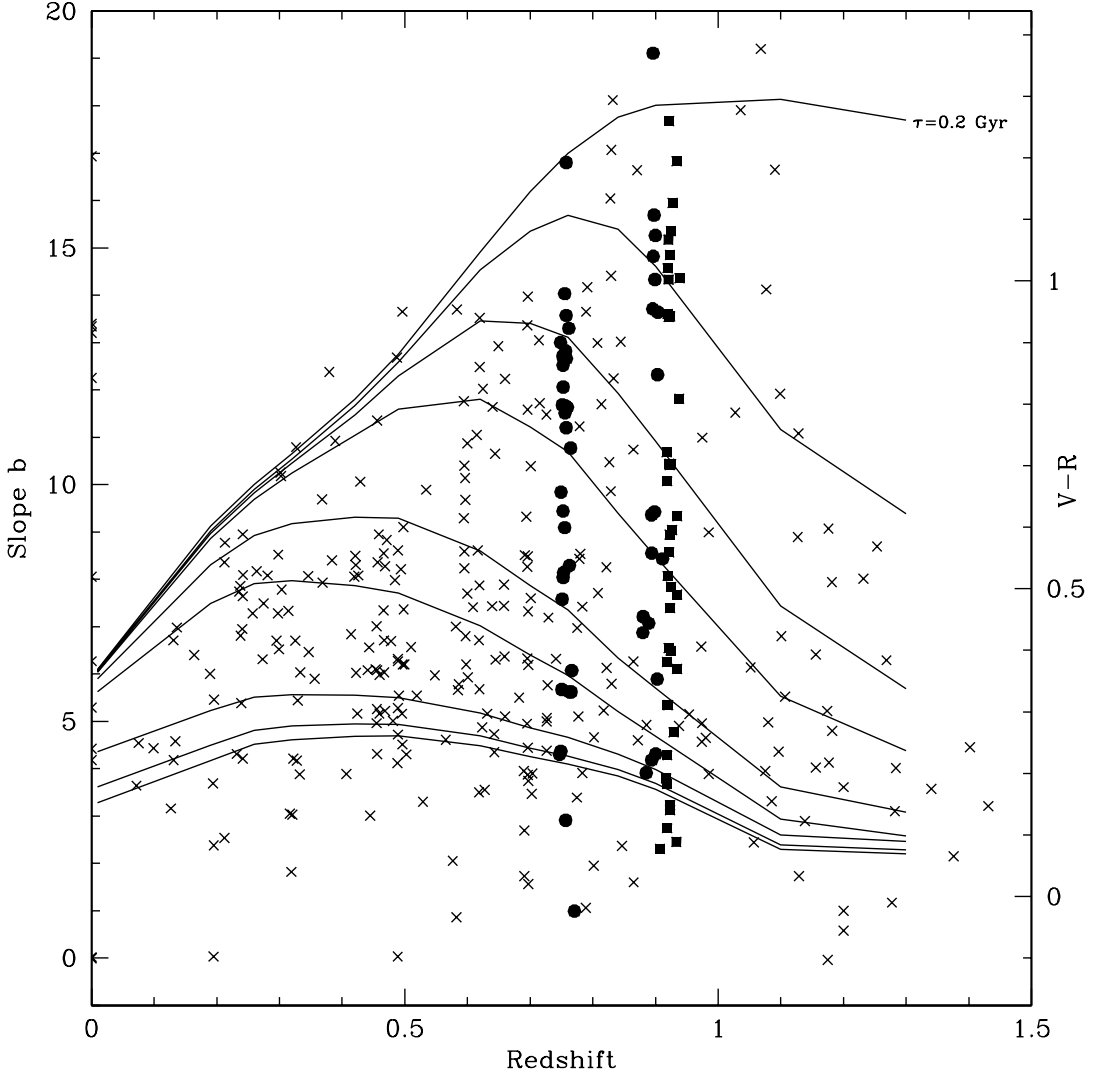


Fig. 12.— A plot of the slope b versus redshift. Cluster members are shown as solid points, field galaxies as crosses. The relationship between age and redshift are calculated based on a Friedman model with $H_o = 65$ and a value of $q_o = 0.1$. It is assumed that star formation commenced 1.05 Gyr after the universe began. Each curve represents the predicted evolution of a galaxy that follows various tau models. From top to bottom the curves correspond to tau0.2, tau0.6, tau0.8, tau1.0, tau1.5, tau2.0, tau5.0, tau10.0, and tau20.0. The righthand ordinate is an approximate $V - R$ color scale.

apparent magnitude. There is no preference for galaxies with equivalent widths greater than 15\AA to lie near the survey magnitude limit. Second, the upper plot in Figure 13 shows the $V - R$ color distributions for the 91 spectroscopically confirmed cluster members (in all three clusters) and for all 1239 objects without spectroscopic observations that have R magnitudes in the *same* range as the confirmed cluster galaxies. A Kolmogorov - Smirnov test indicates that these two distributions are only marginally inconsistent - the hypothesis that the two distributions are drawn from the same parent population is rejected at the 90% confidence level. This is less than a 2σ difference. The source of this small difference is a red tail ($V - R \geq 1.75$) in the $V - R$ distribution in the objects without spectra. As shown in Figure 14 (see below), there is a rough correlation between [OII] equivalent width and galaxy color. If the objects that were not targeted for spectroscopy were preferentially low [OII] emitters, one might expect the distribution of $V - R$ colors in the unmeasured sample to contain a higher fraction of red objects than the spectroscopic sample. The objects with $V - R \geq 1.75$ comprise $\sim 13\%$ of all unobserved objects. However, these reddest objects are distributed relatively uniformly across the imaged areas and are not clustered about the centers of the clusters. It is thus unlikely that they are all cluster members. Only 10% of the spectroscopically unmeasured objects that lie within $500h_{65}^{-1}$ kpc of the cluster centers are redder than $V - R = 1.75$. A conservative limit to the amplitude of any systematic error in our active fraction would thus be about a $\sim 10\%$ overestimate. The actual systematic error is likely to be significantly smaller. We conclude that our estimates of the active fractions in the field and in the clusters are, thus, not strongly biased by our spectroscopic target selection process.

Star formation in galaxies manifests itself in the rest optical bandpass in two important ways. First, star formation leads to the formation of HII regions which, in turn, generate emission lines and, in particular, the [OII], [OIII], and Balmer lines. Second, star formation generates a population of hot stars that make the observed energy distributions of the galaxies blue. The slope b parameter and the emission line equivalent widths are quantitative measures of star formation. Specifically, the slope b measures the importance of young stars in the spectrum. The equivalent width is the ratio of the star formation rate during the last few million years to the continuum generated by the main sequence over the total history of the galaxy. The rest equivalent widths of the [OII] line as a function of the overall spectral energy distribution as represented by the slope b are displayed in Figure 14 for spectroscopically confirmed members of the clusters CL1324+3011, CL1604+4304, and CL1604+4321. Qualitatively, the results are as expected: galaxies with strong emission are blue (small b) while objects with very little emission are red (large b). The predicted b - [OII] EW relationships for the constant age (4.8 Gyr) and the tau0.6 models are shown as well for $z = 0.90$. For the constant tau models, the sensitivity of the relation to the adopted decay rate of star formation is small, largely because the presence of hot stars and [OII] emission are somewhat coupled. In fact, the curves for $\tau = 0.2$ to $\tau = 3.0$ are almost identical. The models fit the majority of these observations quite well suggesting that the constant age scenario (with variable star formation decay rates) is, on average, a plausible hypothesis. The constant tau models also provide a good fit. Galaxies which lie to the upper

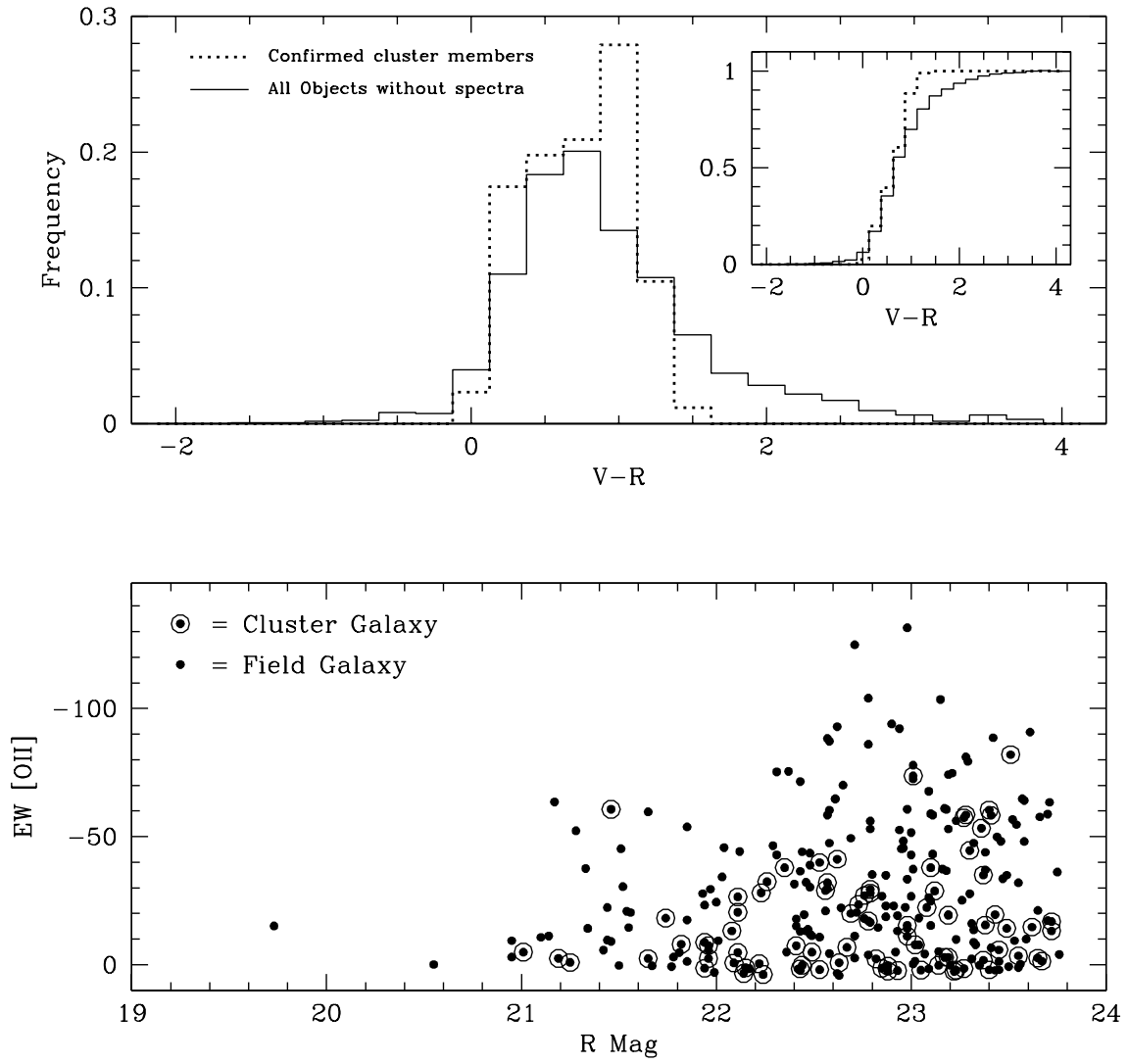


Fig. 13.— Lower plot shows the measured [OII] equivalent width as a function of galaxy R -band magnitude. Cluster members are shown as circled points. Galaxies defined as active ([OII] EW greater than 15Å) are distributed across a broad magnitude range. Upper plot shows the $V - R$ color distributions for the spectroscopically confirmed cluster members and for objects without spectroscopic data (within the same apparent magnitude range as the cluster members).

right of the curves are presumably those systems that have undergone a recent burst of star formation.

There is no indication that the relation between [OII] EW and the slope b in cluster galaxies differs from that in field galaxies. This is as expected since the relationship is controlled largely by the amount of star formation within a given galaxy and not by larger scale environmental conditions.

7.2. Star Formation Rates

We compute model H β intensities and rest equivalent widths by assuming Case B conditions (no Lyman-line photons escape the nebula but are converted into L α or 2-photon plus high level hydrogen line emission) in the ionized gas and use the ionizing flux indicated by the BC96 models in the 230 to 912Å range. It is assumed that there is no 2-photon emission. No reddening corrections are made.

Detailed calculations of the $I([OII])/I(H\beta)$ and $I([OIII])/I(H\beta)$ ratios have been made for example by McCall, Rybski, and Shields (1985). McGaugh (1991) and Olofsson (1997) have concentrated on the combined ratio $(I([OII]) + I([OIII]))/I(H\beta)$. These show that at near-solar oxygen abundances, the $I([OII])/I(H\beta)$ and $(I([OII]) + I([OIII]))/I(H\beta)$ ratios are near a maximum and there is only a small dependence on the oxygen abundance. A factor 10 in abundance difference only produces a factor 1.6 in the intensity ratio. Our observed average ratios $I([OII])/I(H\beta)$ and $I([OIII])/I(H\beta)$ are best fitted with models with about twice the solar O/H ratio. The uncertainty in this number is, however, probably at least a factor 2.

Since the Bruzual and Charlot models are constructed with a known absolute star formation rate, it is straight forward to calculate the equilibrium star formation rate as a function of the emission line intensities. One finds

$$SFR = I(H\beta) \times 1.49 \times 10^{-41} \quad (3)$$

where the intensity, I , is in units of erg s^{-1} and the star formation rate is in $\text{M}_\odot \text{ yr}^{-1}$.

Using the average relation between $I(H\beta)$ and $I([OII])$ and $I(H\beta)$ and $I([OIII])$ from §5.3, one can immediately obtain the SFR using the $I([OII])$ or $I([OIII])$ intensities.

$$SFR = I(O[II]) \times 6.80 \times 10^{-42}. \quad (4)$$

$$SFR = I(O[III]) \times 12.70 \times 10^{-42}. \quad (5)$$

Gallagher, Hunter, & Bushouse (1989) use a constant of 6.5×10^{-42} for the [OII] line while

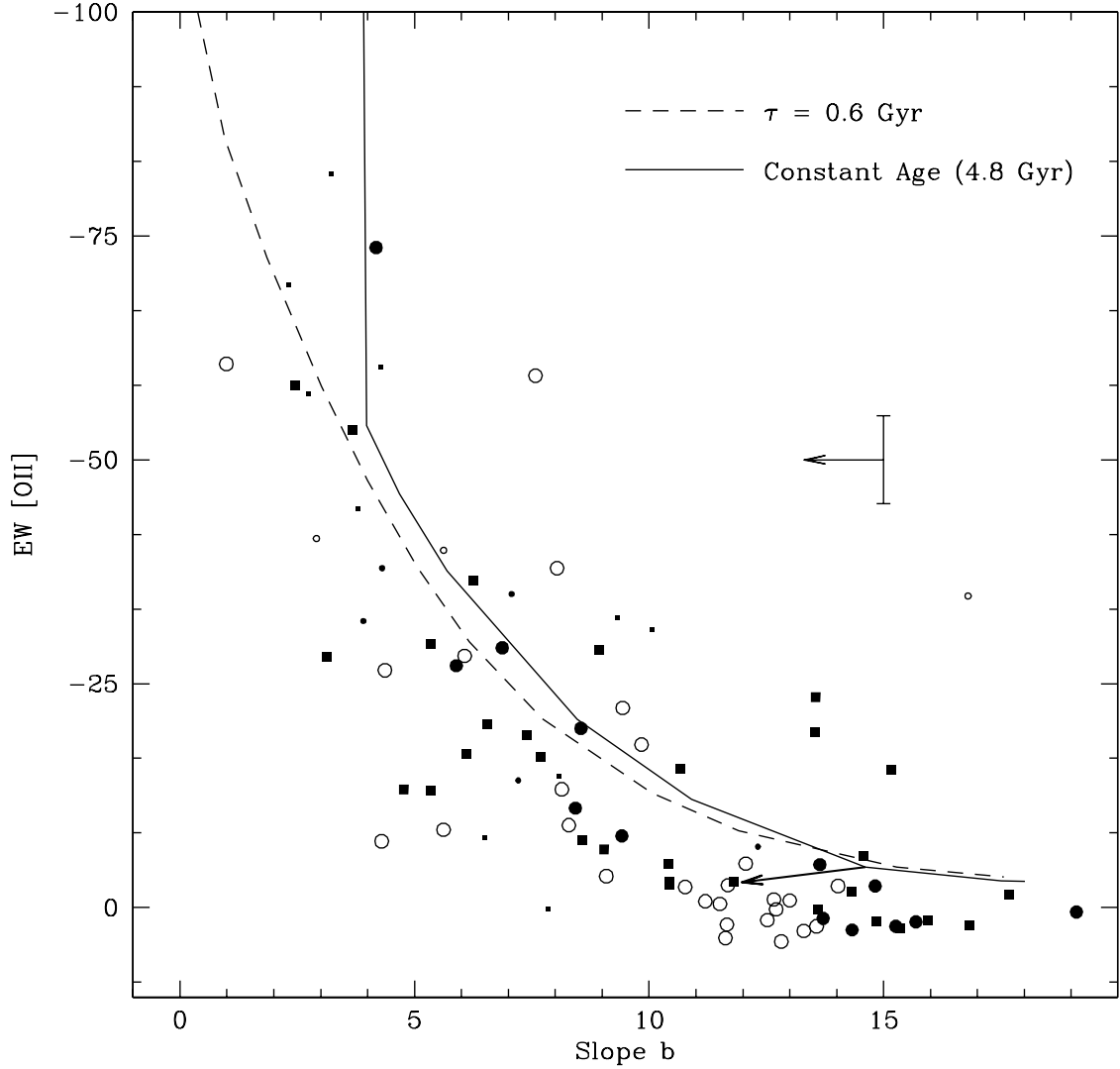


Fig. 14.— The relation between the rest equivalent width (in Angstroms) of the [OII] line and the slope b for confirmed cluster members. The predictions from the Bruzual & Charlot 1996 spectral synthesis package for a solar metallicity model with a constant age (4.8 Gyr at $z = 0.9$) is shown. The symbols are as defined in Figure 8. A typical observation error bar is shown. The observations are shown uncorrected for reddening. The arrow on the error bar shows how the data would shift if corrected for a reddening of $E(B - V) = 0.2$ mag. The diagonal arrow on the model curve shows how the model shifts when the metallicity is reduced to 0.2 solar.

Kennicutt (1992) uses a much larger number 20×10^{-42} . No allowance has been made for foreground reddening. If the reddening corresponds to $E_{B-V} = 0.24$ then the SFR increases by approximately a factor 2.2. The SFR estimates are given in column 17 in Tables 2, 3, and 4. Where possible, the [OII] line has been used; however, in low redshift cases where [OII] is not observed, the H β and [OIII] lines are employed with the [OIII] result being given twice the weight of the H β result since the former line is on average twice as strong as the latter while the continuum uncertainties are comparable.

The SFR increases slowly with increasing redshift up to $z = 0.8$ and exhibits a dramatic increase with redshift above $z = 0.8$. This behavior, shown in Figure 15, is largely a consequence of an increasing *upper* envelope to the SFR with increasing redshift coupled with the loss of intrinsically low luminosity galaxies at higher z due to the survey flux limit. In order to make a less biased study of the SFR across a large range in redshift and absolute luminosity, it is necessary to normalize the SFR value. Ideally, the best normalization would be to divide the SFR by the galaxy mass. Unfortunately, galaxy mass information is not available for this sample. The next best normalizing factor would be the absolute K'-band luminosity. This would work well if the mass-to-light ratio using the K' luminosity was nearly constant. The Bruzual and Charlot models show that this is approximately the case only for a fairly narrow range of models in age and decay time tau. Kelson *et al.* (1997) and van Dokkum *et al.* (1998) find that the V and I band mass-to-light ratios of the early type cluster galaxies have evolved passively since at least $z \sim 1.2$.

K' photometry is only available for the subset of our galaxies which lie within the WFPC2 imaging survey region. To derive K' photometry for the full sample here, it would be necessary to make extrapolations of our BVRI data to K' using the best fit stellar population models. A preferred approach would be to use our *ABB* photometry, which is derived (mostly) by interpolation and, hence, constrained directly by our observations. We can then use the Bruzual and Charlot models and our fits of the observations to these models to determine whether using ABB_{absol} and a normalized star formation rate defined as

$$SFRN = SFR/10^{-0.4(ABB_{absol}+20)} \quad (6)$$

is an acceptable surrogate for a K' based normalization. Using our constant age, variable tau model fits, we calculate the value of ABK'_{absol} using model $ABB_{absol} - ABK'_{absol}$ colors for objects in the CL1604+4304 field. We then calculate a normalized star formation rate $SFRK'$ as defined in the equation above but with ABK'_{absol} . A linear ABK'_{absol} versus ABB_{absol} relation provides a very good fit to the data but the scatter is $\pm 25\%$. The $SFRN - SFRK'$ relation is also linear with a scatter of about $\pm 15\%$. The rare very blue galaxies with $\tau \geq 5.0$ lie significantly beyond this scatter. Had we used constant tau models and allowed the galaxy age to vary, we still would get good linear relations but the scatter would be somewhat larger. For statistical purposes, therefore, it appears that using ABB_{absol} to normalize the SFR is an adequate alternative to a K' based normalization. We note that the equivalent width of the [OII] line is approximately proportional to $SFRN$: $EW[\text{OII}] \approx 27.6 \times SFRN$.

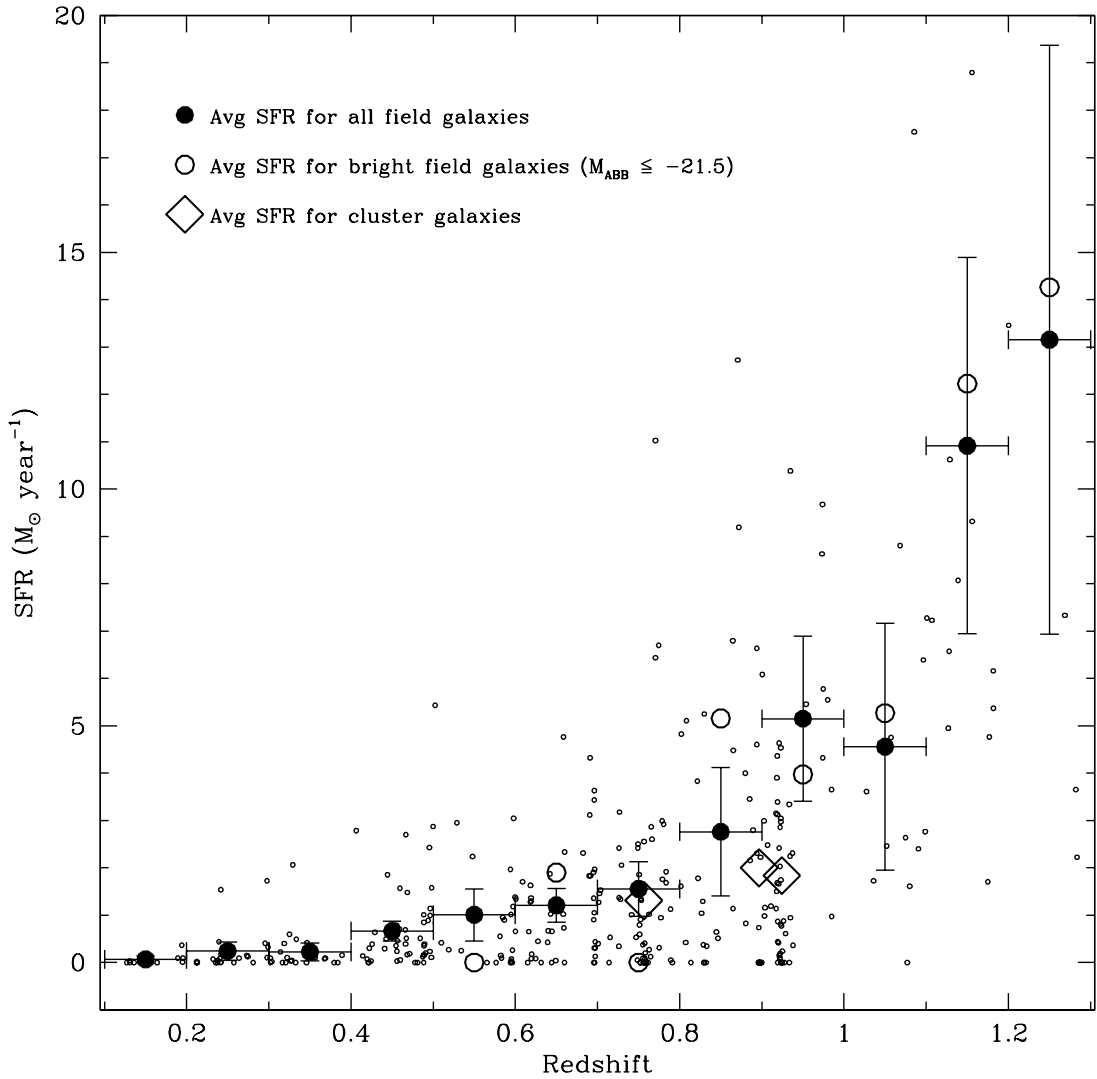


Fig. 15.— The star formation rate, in $M_{\odot} \text{ yr}^{-1}$, as a function of redshift for all galaxies in the sample. The large solid circles (with error bars) are the mean SFR values for field galaxies in redshift intervals of 0.1. The errors are the formal 2σ uncertainties. The large diamond symbols are the mean SFR for the galaxies in all three clusters. The large open circles are the mean SFR values for field galaxies with $z \geq 0.7$ and $M_{ABB} < -21.5$. The small open circles are the SFR data for each galaxy.

A further question is how nearly the luminosity calculated from the K' magnitude is proportional to the mass. Again, using the Bruzual and Charlot models, it is possible to investigate this for the range of models and ages which are relevant. At a given redshift it is found that it does represent the mass with a scatter of $\pm 20 - 30\%$. It does however change systematically with redshift. Between $z = 0.50$ and $z = 1.30$ ABK'_{absol} brightens by 0.53 mag and is linear with z . This is because in our constant age models the galaxies get younger as redshift increases. In a constant tau scenario this effect is not present because there is a range of ages at each redshift.

To investigate how the star formation rate, the normalized star formation rate (SFRN), and the [OII] line equivalent width change with galaxy luminosity and redshift, we have chosen to generate averages in bins corresponding to approximately 0.1 in z and 1 magnitude in luminosity. The luminosity bins allow for the expected evolution in luminosity with redshift. The SFRN results are listed in Table 10 and all three SFR indicators are plotted in Figure 16. There are two general trends: (1) at a given luminosity, both the [OII] EW and the SFRN increase as z increases; (2) at a given redshift, both the [OII] EW and the SFRN decrease as the luminosity increases. The remarkable aspect of this latter trend is the uniformity of the nearly linear decline in SFRN with increasing ABB luminosity for galaxies with $z \lesssim 0.9$. This result implies that, on average, the SFR is effectively independent of galaxy luminosity over the range $-18 \geq \text{ABB} \geq -22$. This is explicitly demonstrated in the upper plot of Figure 16. Sullivan *et al.* (2000) find a similarly weak dependence of [OII] equivalent width on galaxy luminosity at $z < 0.2$.

The increase in SFRN with redshift, at a fixed ABB luminosity, is consistent with the predictions of our BC model fits. Naturally, there are important differences between galaxies with different spectral and photometric characteristics. For example, one expects the SFRN to be dependent on the color of the galaxy, being larger for galaxies which are bluer. Since the equivalent width of [OII] is approximately proportional to SFRN, the result is very much like that in Figure 14. In the clusters in particular, for slope $b \geq 11$, the average SFRN is 0.20 while for $b < 5$, every object has $\text{SFRN} > 1.0$. Red objects have very little star formation while in blue objects the star formation rate is high. One obtains a similar result from the spectral classifications. The average values of SFRN are 1.56, 0.79, 0.61, and 0.25, respectively, for spectral classes “ a ”, “ $a+k$ ”, “ $k+a$ ”, and “ k ”.

8. Cluster Structure

Cluster formation is believed to involve both a significant amount of infall of the surrounding field galaxies into the cluster’s potential as well as environmental processing of the cluster members as they undergo ram pressure stripping, tidal disruption, and merging. This hypothesis predicts that there should be correlations between the spectral properties of the cluster members and their clustocentric distance. The amplitude of the correlations tell us something about the fraction of cluster members which have been recently accreted and/or

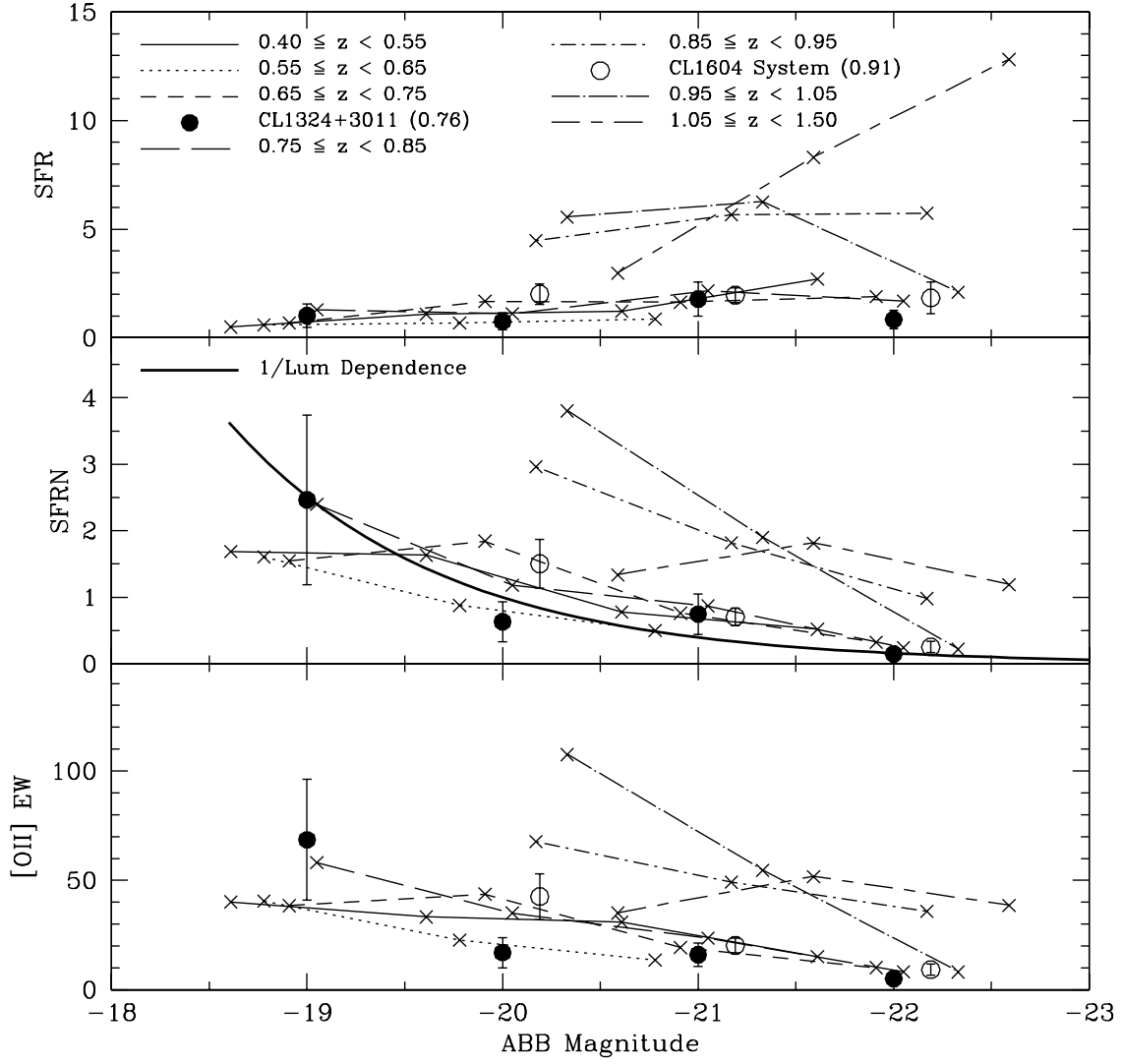


Fig. 16.— Various star formation indicators as a function of ABB magnitude and redshift. The upper plot shows the direct star formation rate ($M_{\odot} \text{ yr}^{-1}$); the middle plot shows the normalized star formation rate, SFRN in units of $M_{\odot} \text{ yr}^{-1}$ per unit ABB luminosity, and the lower plot shows the absolute value of the [OII] line equivalent width (in Å). Data for field galaxies are plotted as lines, data for the cluster members are shown as points with 1σ errors (the CL1604 system results include data for CL1604+4304 and CL1604+4321). In the SFRN vs ABB plot, the heavy solid line is the trend expected for a fixed star formation rate.

the degree to which environmental processes alter the galaxy characteristics. Figure 17 shows the distribution of galaxy spectral class as a function of the comoving clustocentric distance. Galaxies of spectral class “ k ” appear to be somewhat more centrally concentrated than the bluer galaxies of spectral classes “ a ” and “ $a+k$ ”. The difference, however, is not significant in our current sample. A KS test yields a 42% probability that galaxies with spectral class “ k ” are drawn from the same spatial distribution as those with spectral classes “ a ” or “ $a+k$ ”. However, the factor of ~ 3 decline in the fraction of “ k ”-type galaxies as the clustocentric radius increases from $250h_{65}^{-1}$ kpc to $1.5h_{65}^{-1}$ Mpc is significant.

We can also look at the values of the SFR and SFRN as functions of the projected distance of a galaxy from the cluster center. The data are shown in Figure 18. The data for the three clusters are shown on the left side of the figure. On the right side, for comparison, are the SFR and SFRN values for field galaxies in the redshift range $0.65 \leq z \leq 1.00$. For comoving clustocentric radii less than $1h_{65}^{-1}$ Mpc, a large majority of the cluster objects have low SFRN relative to their field galaxy counterparts. At large distances there are very few low SFRN objects. The few high SFRN objects projected near the center of the cluster could be outliers in the distribution, recently infalling galaxies, or foreground and background objects, although their redshifts are consistent with their being cluster members. A comparison of the cluster galaxies at large distances and field galaxies shows them to be quite similar, although the cluster numbers are quite small. Similar results have been produced for clusters and field galaxies with redshifts from 0.18 to 0.55 by Balogh *et al.* (1997), Morris *et al.* (1998), Balogh *et al.* (1998), and Balogh *et al.* (1999). They find the same suppression of the SFR in clusters relative to the field at the same redshifts. They suggest that this is caused by ram pressure or tidal stripping of the gas from galaxies as they first fall into the cluster potential or pass near the cluster center. Balogh *et al.* (1998) find that even in the outer regions of the clusters the SFR is less than in the field whereas our data suggest that they are much the same. This may be an evolutionary effect in which the process of suppression of the SFR in clusters has proceeded further at $z = 0.5$ than at the much earlier time corresponding to $z = 0.9$. Larger surveys, sampling systems with a broad range in ICM properties, are needed to fully understand the nature of the observed trends.

9. Conclusions

Extensive data from a joint HST/Keck imaging and spectroscopic survey of 9 distant clusters has provided a wealth of observational constraints on galaxy and cluster evolution. In this paper, we have focused on the properties of the galaxies in and around the 3 most massive clusters in our survey: CL1324+3011 ($z = 0.757$), CL1604+4304 ($z = 0.897$), and CL1604+4321 ($z = 0.924$). Our most important results are summarized below.

- The central velocity dispersions of the clusters are accurately measured from the redshifts of ~ 20 to 40 member galaxies. The dispersions lie in the range $900 - 1300$ km s $^{-1}$ and the resulting kinematic mass estimates are $\gtrsim 5 \times 10^{14}h_{65}^{-1}$ M $_{\odot}$ (see Table 5 and

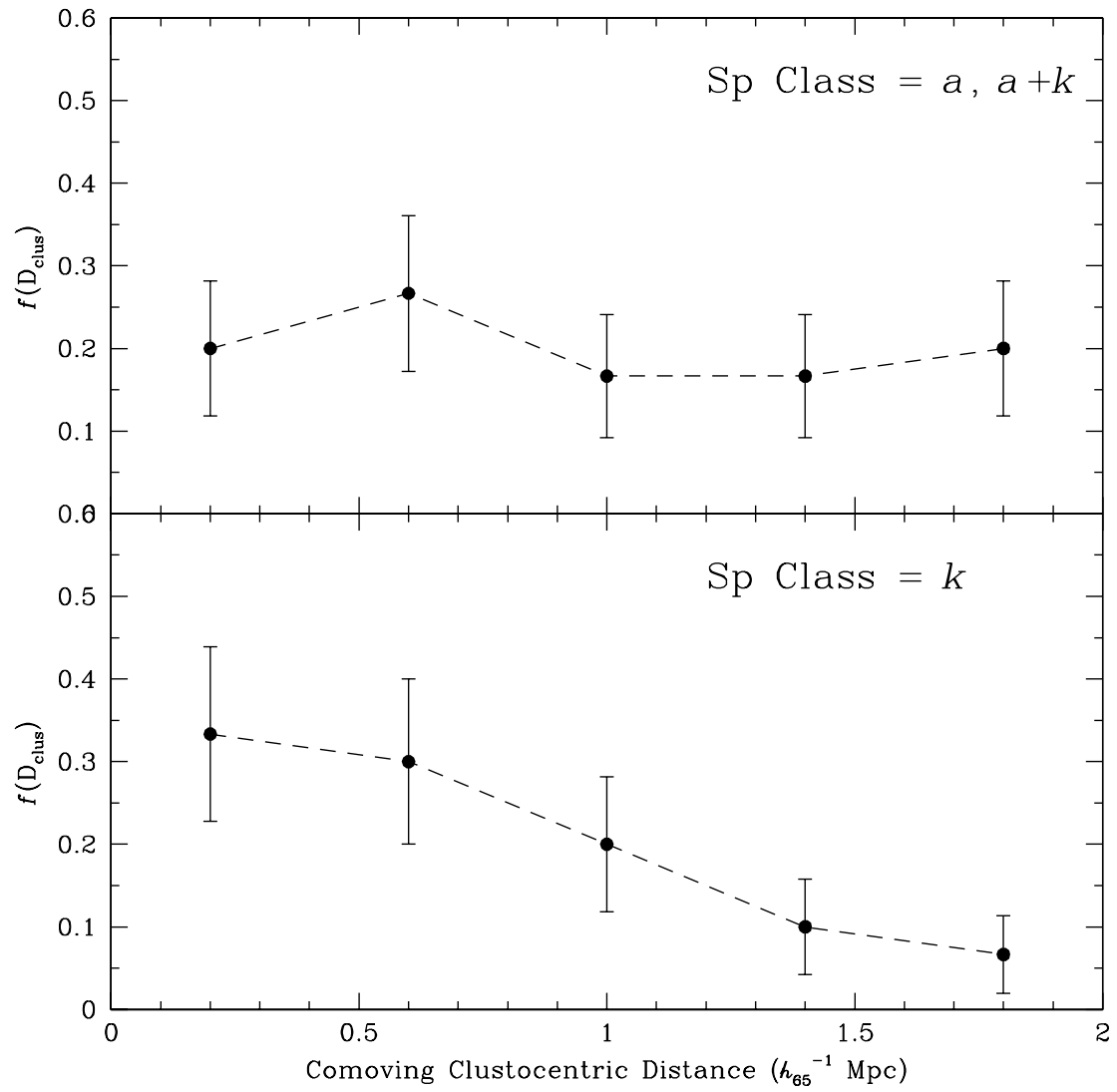


Fig. 17.— The distribution of galaxy spectral type as a function of the comoving clustocentric radius. Data for all three clusters are combined in this figure.

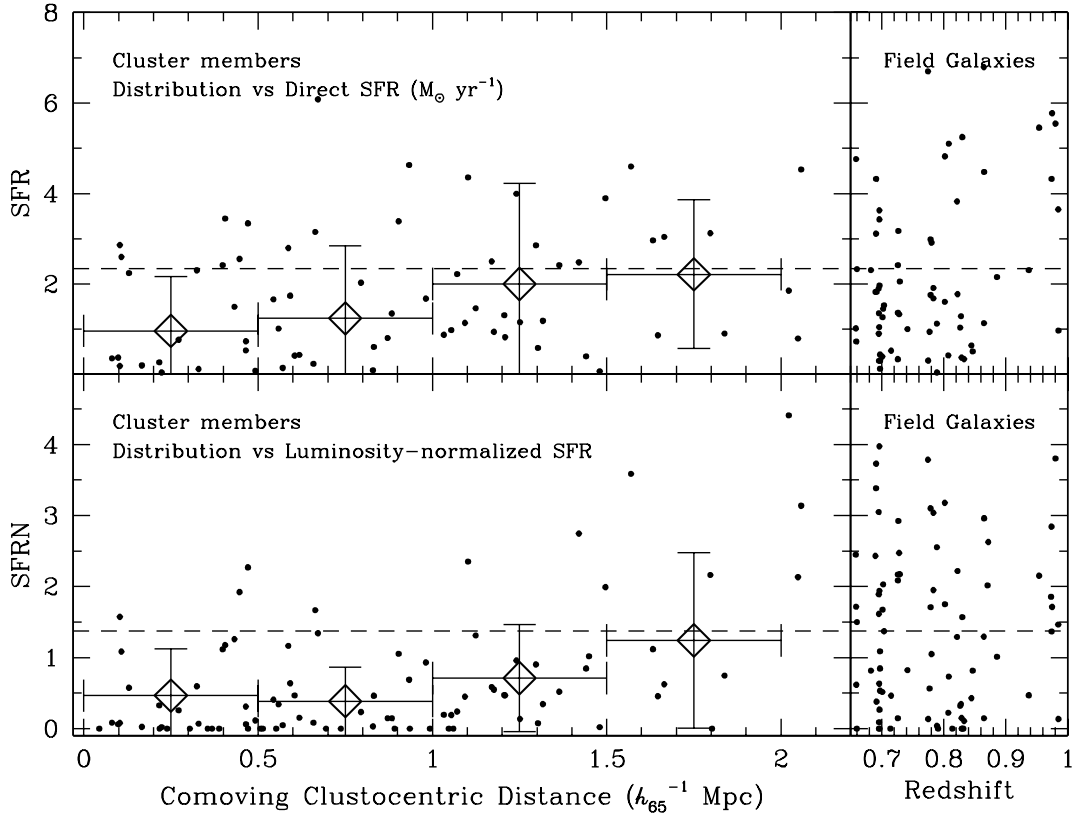


Fig. 18.— The direct star formation rate, SFR (upper plot), and the normalized star formation rate, SFRN (lower plot), as functions of the comoving clustocentric radius. The large diamonds show the mean values in four ($500h_{65}^{-1}$ kpc) radial bins. The trends for both these measures of star formation are similar. Vertical errors on the large diamonds indicate the standard deviation about the mean, horizontal errors show the radial bin size. The small points are the data for individual objects. Also shown, at right, are the SFR and SFRN as functions of redshift for field galaxies at redshifts similar to those of the clusters ($0.65 \leq z \leq 1$). The dashed lines are the mean SFR and SFRN values for the field galaxies.

Figure 3). The bolometric x-ray luminosities of these clusters are: $\log(L_{x,Bol}) = 43.95$ for CL1324+3011, $\log(L_{x,Bol}) = 44.05$ for CL1604+4304, and $\log(L_{x,Bol}) \leq 43.90$ for CL1604+4321 (the uncertainties in the logarithm of the bolometric luminosity are about ± 0.5). These values are low for the derived velocity dispersions of these clusters. For example, the low- z $\sigma - T_x$ relation (Donahue *et al.* 1998) would predict our clusters should have kinetic ICM temperatures in the range 5 – 10 keV, suggesting bolometric x-ray luminosities in excess of 10^{45} erg s $^{-1}$ (based on the $L_x - T_x$ relation from Mushotzky & Scharf 1997). Specifically, the predicted bolometric luminosities based on the Mushotzky & Scharf results⁵ are $\log(L_{x,Bol}) = 45.0, 45.4$, and 44.7 for CL1324+3011, CL1604+4304, and CL1604+4321, respectively – about an order of magnitude larger than what is actually observed (the factor can lie in the range 3 to 60, depending on the cluster, due to the error in the observed quantity). However, this is not uncommon in optically selected clusters at $z > 0.7$ (*e.g.*, see Holden *et al.* 1997). Possible explanations for this may include an enhanced population of optically rich, x-ray faint clusters at $z > 0.6$, more efficient detection of galaxy-rich clusters in which the dynamical state of the ICM is still evolving when selecting clusters in optical passbands, and a higher fraction of clusters at $z \sim 0.8$ in which the infall of field galaxies is still a significant process.

- The cluster M/L ratios are consistent with those derived for their low- z counterparts, lying comfortably between 100 – 500 (see Table 6). The systematic errors associated with determining these ratios prevent any conclusive statements about evolution of the M/L ratios. However, large M/L (> 1300) ratios, expected if $\Omega_m = 1$ on cluster scales, are strongly ($> 99\%$ C.L.) rejected.
- The rest-frame B-band characteristic magnitude of the integrated field galaxy luminosity function evolves with redshift roughly as $M^*(z) = M^*(0) - \beta z$ where $1 < \beta < 1.5$ (see Table 7 and Figures 4 and 5). Caution is recommended in the interpretation of this observation as we do not have a sufficient number of objects to subdivide our analysis by galaxy color or spectral class. It is well known that the local LF is a strong function of color (*e.g.*, Blanton *et al.* 2001) and evolution of the LF has already been shown to be color dependent (*e.g.*, Lilly *et al.* 1995). We note, however, the our observations of the brightest cluster galaxies show that their rest-frame B-band luminosity evolves with redshift in a very similar fashion. The tau0.2 model predicts an increase in BCG luminosity which is nearly identical to the simple LF evolution with $\beta = 1$; the tau1.0 model for BCG evolution is nearly identical to the $\beta = 1.5$ scenario. The observed evolution of the absolute BCG magnitudes is best fit by solar metallicity models with $0.2 \lesssim \tau < 0.6$. Our data also suggest that the M_{ABB}^* in clusters has dimmed by about 0.7 mag between $z \sim 0.8$ and the current epoch.

⁵The values of the predicted bolometric luminosity are derived by taking the mean of the least square fits using $L_{x,Bol}$ and then T_x as the independent variable.

- The mean spectral characteristics of the cluster galaxies, such as the metal-line equivalent widths, J_u jump parameter, and derived (normalized) star formation rates, are well correlated with their broadband photometric properties, such as the slope b value (see Table 8 and Figures 7, 8, 10, and 14). These correlations are a straight forward consequence of the star formation process – galaxies with active star forming regions have spectra with oxygen line emission and Balmer absorption. These same galaxies have blue SEDs as a consequence of their young stellar population. Similarly, the light from older galaxies, which typically have strong metal-line absorption features, is dominated by a red stellar population. These correlations are also observed in field galaxies.
- The spectroscopic and photometric properties of the cluster galaxies are well fit by the Bruzual-Charlot solar metallicity, constant-age (4.8 Gyr at $z = 0.9$), variable tau models. Models with sub-solar metallicity are not strongly rejected so long as long as the metallicity is at least 0.2 of solar. A significant amount of dust extinction at $z \sim 0.9$ is not likely – the observations can be fit acceptably by the solar metallicity models so long as $E(B - V) \lesssim 0.2$ mag.
- All the clusters host a significant early-type galaxy population, although an envelope of red elliptical-like galaxies, so prominent in many $z \leq 0.5$ clusters, is only weakly detected at these redshifts (see Figures 1 and 12). Indeed, many of the spectroscopically confirmed cluster members are blue (slope $b < 7$, $V - R < 0.5$) and some remarkably so ($V - R \approx 0$). These observations are consistent with the predictions from coeval tau models: the intrinsic scatter in the logarithmic slope of the (optical) spectral energy distributions of the redder cluster members is expected to decrease by a factor ~ 2 between $z = 0.9$ and $z = 0.5$ and by a further factor of ~ 2 between $z = 0.5$ and the current epoch. We note that the contrast of the red elliptical sequence is enhanced significantly if a NIR passband is combined with an optical passband in the definition of the CM diagram (*e.g.*, Gladders & Yee 2000).
- The average $I([OII])/I(H\beta)$ ratio is very similar to that found in nearby galaxies while the average $I([OIII])/I(H\beta)$ is somewhat higher. These ratios are best fit by models with a metallicity of twice solar, although the uncertainty is at least a factor 2.
- A star formation rate, SFRN, normalized to the galaxy’s luminosity at the rest B wavelength, is found to increase as the redshift increases and decrease as the luminosity increases (see Table 10 and Figure 16). In addition, models show that, on average, the SFRN is predicted to be roughly proportional to the SFR per unit mass our sample of galaxies. The SFR and SFRN are correlated with galaxy color and spectral classification – redder galaxies exhibit, on average, weaker star formation activity and stronger metal line absorption. One remarkable aspect of these results is the uniformity of the decline of SFRN with luminosity over a large range of ABB magnitude and redshift. This implies that the average SFR per galaxy in this sample is nearly independent of galaxy redshift and luminosity in the ranges $0.4 \lesssim z \lesssim 0.9$ and $-18 \geq ABB \geq -22$.

- For field galaxies with $0.40 < z \leq 0.85$, 65% are active ([OII] equivalent width greater than 15\AA). For field galaxies with $z > 0.85$, the fraction is 79%. Within the central $1.5 h_{65}^{-1}$ Mpc regions of our three distant clusters, the fraction of active galaxies is 45%. This is substantially higher than the 10 to 20% active galaxy component seen in the centers of $0.2 < z < 0.55$ clusters but is lower than that seen in the field at redshifts comparable with those of our distant clusters. Within the central comoving cluster distance of $1.0 h_{65}^{-1}$ Mpc a large fraction of the cluster galaxies have low values of SFRN (relative to field galaxies at similar redshifts) and have spectra which exhibit strong CaII K, $\lambda 3835$ and g-band absorption but exhibit little or no H γ absorption. Above $1.0 h_{65}^{-1}$ Mpc, on the other hand, the average SFRN in cluster galaxies is nearly as high as that in field galaxies in the same redshift range. The smooth melding of the star forming properties of galaxies in the outskirts of the clusters with that in galaxies in the general field (see Figure 18) coupled with the lower overall fraction of active galaxies in the cluster cores can be understood if a) the accretion of field galaxies by the clusters is a significant process at these intermediate redshifts and/or b) if the volume containing the majority of gas-poor cluster members (due to environmental processes such as ram pressure stripping) evolves with time. In the latter case, we would conclude that at $z \sim 0.8$ the effects of cluster induced gas stripping have been largely confined to the central $1 h_{65}^{-1}$ Mpc region whereas at $z < 0.5$ the effects of these processes encompass a significantly larger volume about the cluster center (*e.g.*, Balogh *et al.* 1998).
- We detect a factor of ~ 3 decline in the fraction of “ k ”-type galaxies as the clustocentric radius increases from $250 h_{65}^{-1}$ kpc to $1.5 h_{65}^{-1}$ Mpc (see Figure 17). This is further evidence in support of the importance of environmental effects in cluster cores on star formation activity in galaxies. However, a similar trend would be expected in a hierarchical structure formation scenario in which the most massive galaxies form first and are thus the oldest (and, hence, most centrally located) members of the cluster.

LML is supported by NASA through Hubble Fellowship grant HF-01095.01-97A from the Space Telescope Science Institute, which is operated by the Association of Universities for Research in Astronomy, Inc., under NASA contract NAS 5-26555.

Observational material for this paper was obtained at the W. M. Keck Observatory, which is operated as a scientific partnership between the California Institute of Technology, the University of California, and the National Aeronautics and Space Administration. It was made possible by the generous financial support of the W. M. Keck Foundation.

REFERENCES

Adami, C., Biviano, A., Mazure, A. 1998, A&A, 331, 439

Aragón-Salamanca, A., Ellis, R.S., Couch, W.J. & Carter, D. 1993, MNRAS, 262, 764

Bahcall, J.N., & Tremaine, S. 1981, ApJ, 244, 805

Balogh, M.L., Morris, S.L., Yee, H.K.C., Carlberg, R.G., & Ellingson, E. 1997, ApJ, 488, L75.

Balogh, M. L., Schade, D., Morris, S. L., Yee, H. K. C., Carlberg, R. G., & Ellingson, E. 1998, ApJ, 504, L75.

Balogh, M. L., Morris, S. L., Yee, H. K. C., Carlberg, R. G., & Ellingson, E. 1999, ApJ, 527, 54.

Barger, A.J., Aragón-Salamanca, A., Ellis, R.S., Couch, W.J., Smail, I., & Sharples, R.M. 1996, MNRAS, 279, 1.

Beers, T.C., Flynn, K., & Gebhardt, K. 1990, AJ, 100, 32.

Bertin, E., Arnouts, S. 1996, A&AS, 117, 393.

Blanton, M. R. *et al.* , 2000, BAAS, 197, 2703

Bower, R. G., Kodama, T., Terlevich, A. 1998, MNRAS, , 299, 1193

Brunner, R.J., Connolly, A.J., & Szalay, A.S. 1999, ApJ, 516, 563

Bruzual, A. C. & Charlot, S. 1993, ApJ, 405, 538.

Carlberg, R.G., Yee, H.K.C., Ellingson, E., Abraham, R., Gravel, P., Morris, S., & Pritchett, C.J. 1996, ApJ, 462, 32

Castander, F. J., Ellis, R. S., Frenk, C. S., Dressler, A., & Gunn, J. E. 1994, ApJ, 424, L79

Colless, M. 1989, MNRAS, , 237, 799

Couch, W.J., Ellis, R. S., McLaren, I., Malin, D. F. 1991, MNRAS, , 249, 606

Donahue, M, Voit, G. M, Gioia, I, Lupino, G, Hughes, J. P., Stocke, J. T. 1998, ApJ, , 502, 550

Dressler, A., & Gunn, J.E. 1992, ApJS, 78,1

Dressler, A., Oemler, A., Couch, W. J., Smail, I, Ellis, R. S., Barger, A., Butcher, H, Poggianti, B. M., Sharples, R. M. 1997, ApJ, , 490, 577

Dressler, A., Smail, I., Poggianti, B. M., Butcher, H., Couch, W. J., Ellis, R. S., Oemler, A., 1999, ApJS, 122, 51

Edge, A. C., Stewart, G. C. 1991, MNRAS, 252, 414.

Ellis, R. S., Smail, I., Dressler, A., Couch, W. A., Oemler, A., Butcher, H., Sharples, R. M. 1997, ApJ, , 483, 582

Gallagher, J. S., Hunter, D. A., Bushouse, H. 1989, AJ, , 97, 700

Gioia, I. A., Henry, J. P., Mullis, C. R., Ebeling, H. 1999, AJ, , 117, 2608

Girardi, M., Borgani, S., Giuricin, G., Mardirossian, F., Mezzetti, M. 2000, ApJ, 530, 62.

Gladders, M. D. 2000, BAAS, 197, 5703

Gladders, M. D., & Yee, H. K. C. 2000, AJ, 120, 2148.

Gonzales, A., Zaritsky, D., Dalcanton, J., Nelson, A. 2001, ApJ, submitted

Gunn, J. E., & Oke, J. B. 1975, ApJ, 195, 255.

Hammer, F., Flores, H., Lilly, S.J., Crampton, D., Le Fevre, O., Rola, C., Mallen-Ornelas, G., Schade, D., & Tresse, L. 1997, ApJ, 481, 49

Heisler, J., Tremaine, S., & Bahcall, J.N. 1985, ApJ, 298, 8

Holden, B. P., Romer, A. K., Nichol, R. C., & Ulmer, M. P. 1997, AJ, 114, 1701

Kelson, D., van Dokkum, P., Franx, M., Illingworth, G., Fabricant, D. 1997, ApJ, 478, L13

Kennicutt, R. 1992, ApJ, 388, 310.

Lilly, S. J., Tresse, L., Hammer, F., Crampton, D., Le Fevre, O. 1995, ApJ, 455, 108.

Lubin, L. M., & Postman, M. 1996, AJ, 111, 1795

Lubin, L. M., Postman, M., Oke, J. B., Gunn, J. E., Hoessel, J. G., Schneider, D. P. 1998, AJ, 116, 584 [Paper III]

Lubin, L.M., Brunner, R., Metzger, M.R., Postman, M., & Oke, J. B., 2000, ApJ, 531, L1.

Lubin, L. M. *et al.* 2001, [Paper V]

Lumsden, S. L., Collins, C. A., Nichol, R. C., Eke, V. R., & Guzzo, L. 1997, MNRAS, , 290, 119

McCall, M. L., Rybski, P. M., Shields, G. A. 1985, ApJS, 57, 1.

McGaugh, S. S. 1991, ApJ, 380, 140.

Morris, S. L., Hutchings, J. B., Carlberg, R. G., Yee, H. K. C., Ellingson, E., Balogh, M. L., Abraham, R. G., Smecker-Hane, T. A. 1998, *ApJ*, 507, 84.

Mushotzky, R. F. & Scharf, C. A. 1997, *ApJ*, 485, L13

Oke, J. B. et al. 1995, *PASP*, 107, 375.

Oke, J. B., Gunn, J. E., Hoessel, J. G. 1996, *AJ*, 111, 290.

Oke, J. B., Postman, M., Lubin, L. M. 1998, *AJ*, 116, 549 [Paper I]

Olofsson, K. 1997, *A&A*, 321, 29.

Poggianti, B. M., Smail, I., Dressler, A., Couch, W. J., Barger, A. J., Butcher, H., Ellis, R. S., Oemler, A. 1999, *ApJ*, 518, 576

Postman, M. & Lauer, T. R. 1995, *ApJ*, 440, 28.

Postman, M., Lubin, L. M., Oke, J. B. 1998, *AJ*, 116, 560 [Paper II]

Postman, M., Lauer, T., Oegerle, W. 2001, *ApJ*, , submitted

Rauzy, S., Adami, C., & Mazure, A. 1998, *A&A*, 337, 31

Schechter, P. 1976, *ApJ*, 203, 297.

Smail, I., Ellis, R.S. & Fitchett, M.J. 1994, *MNRAS*, 270, 245

Smail, I., Dressler, A., Couch, W. J., Ellis, R. S., Oemler, A., Butcher, H., Sharples, R. M. 1997 *ApJS*, 110, 213

Small, T. A., Ma, C., Sargent, W., Hamilton, D. 1998, *ApJ*, 492, 45.

Stanford, S. A., Eisenhardt, P. R., Dickinson, M. 1995, *ApJ*, 450, 512

Stanford, S. A., Eisenhardt, P. R., Dickinson, M. 1998, *ApJ*, 492, 461.

Sullivan, M., Treyer, M. A., Ellis, R. S., Bridges, T. J., Milliard, B., Donas, J. 2000, *MNRAS*, 312, 442.

Valdes, F. 1982, *Proc. SPIE*, 331, 465.

Valotto, C. A., Nicotra, M. A., Muriel, H., & Lambas, D. G. 1997, *ApJ*, , 479, 90

van Dokkum, P., Franx, M., Kelson, D., Illingworth, G. 1998, *ApJ*, 504, L17

van Dokkum, P., Franx, M., Fabricant, D., Illingworth, G., Kelson, D. 2000, *ApJ*, 541, 95

van Dokkum, P. & Franx, M. 2001, *astro-ph/0101468*

van Zee, L., Salzer, J. J., Haynes, M. P. 1998, ApJ, 497, L1.

Table 1. Summary of Spectroscopic Observations

	Cl1324+3011	CL1604+4321
(1) Number in mag-limited sample	215	227
(2) Number not observed	54	48
(3) Number observed, no result	14	28
(4) Number of $z=0.0000$ cases	12	16
(5) Number with significant redshifts(including 1 QSO)	135	135
(6) Number in (5) with emission lines	104	106

Table 2. Photometric and Spectroscopic Data for Field CL1324+3011

Table 2—Continued

ID#	AB_B	AB_V	AB_R	AB_I	z	Q	b	tau	Sp	Age		J_l	J_u	SFR	M_{ABB}		
										$\tau_{0.6}$	[OII]	$H\beta$	[OIII]				
* 1767	24.58	23.88	23.30	22.34	0.7527	4	8.04	1.4	a+k	2.6	-37.9	-11.2	-26.5	0.28	0.09	1.47	-20.12
1785	23.43	22.88	22.63	22.21	0.5025	4	4.30	long	...	1.1	...	-26.8	-143.0	...	0.06	5.43	-19.27
1793	24.48	23.09	22.22	21.11	0.5342	4	9.89	1.1	k	5.0	-9.4	1.0	-4.5	0.58	0.41	0.25	-19.97
1817	23.85	23.61	23.28	22.87	1.3400	3	3.57	0.9	...	2.2	-26.2	6.57	-22.23
1831	24.38	23.95	23.63	23.95	9.0000	0	3.33
1869	23.85	23.39	23.04	22.49	0.8858	4	4.92	1.9	k+a	1.8	-26.8	0.51	0.22	2.15	-20.82
1884	24.69	22.81	21.71	20.28	0.6597	4	12.23	0.2	k	7.0	0.3	2.9	1.3	0.46	0.50	0.00	-21.40
1952	0.4886	3	0.03	long	k+a	0.2	...	-0.5	3.8	...	0.46	0.00	...
1957	24.27	24.14	23.69	23.66	0.3206	2	3.03	long	a	0.6	0.7	2.1	0.8	0.24	0.24	0.00	-17.07
* 1990	26.91	24.58	23.45	21.87	0.7576	4	13.57	0.4	k	5.0	2.1	-1.5	-3.4	0.46	0.44	0.00	-20.37
2029	23.70	23.43	23.41	22.75	9.0000	0	2.93
2057	24.46	24.26	24.26	22.87	0.5866	2	5.78	2.0	...	1.7	-82.7	-16.0	-18.6	1.15	0.35	0.90	-18.57
2073	24.00	23.75	23.16	22.46	0.5848	4	5.66	2.0	a	1.7	-48.3	-5.5	-13.8	0.71	0.26	0.95	-19.22
2079	23.88	23.25	22.58	21.38	9.0000	0	9.54
2083	23.84	23.25	22.97	22.40	0.4810	4	5.01	10.0	a	1.4	20.8	-3.0	-21.8	...	0.18	0.00	-18.85
* 2114	22.92	22.57	22.13	21.37	0.7627	4	5.62	2.0	a+k	1.7	-8.7	2.7	-3.5	0.34	0.15	1.02	-21.18
** 2151	23.68	22.27	21.22	19.82	0.7528	4	12.06	0.9	k	4.0	-4.9	6.3	1.5	0.52	0.53	1.35	-22.43
2171	...	24.57	23.69	21.37	0.0000	4
* 2186	23.13	22.88	22.60	21.89	0.7470	4	4.30	5.0	a+k	1.4	-7.4	2.7	6.3	0.51	0.18	0.53	-20.59
2189	23.34	23.00	22.72	22.05	9.0000	0	4.50
2192	23.10	22.55	22.04	21.70	0.4685	4	5.22	10.0	a+k	1.6	-53.8	-6.4	-13.1	0.78	0.25	1.48	-19.64
2235	24.24	23.91	23.93	23.60	9.0000	0	2.03
* 2253	22.94	22.73	22.30	21.74	0.7490	4	4.37	5.0	a	1.4	-26.5	-9.1	-9.4	0.47	0.11	2.42	-20.84
* 2279	24.61	23.18	22.15	20.68	0.7524	4	12.52	0.7	k	5.0	1.4	7.0	6.8	0.43	0.48	0.00	-21.57
* 2310	24.95	23.94	23.03	21.79	0.7646	4	10.77	1.1	a+k	3.5	-2.3	7.6	-10.8	0.70	0.32	0.12	-20.59
* 2331	23.12	22.98	22.80	22.20	0.7567	1	2.91	long	a	0.9	-41.2	0.28	0.14	2.56	-20.31
2332	23.47	22.46	21.81	20.94	0.0000	4	8.05
2357	23.51	23.20	23.08	22.28	1.1556	4	4.02	1.1	...	2.0	-94.0	1.51	0.35	18.80	-21.88
2373	24.71	24.65	25.22	23.52	0.6973	4	3.74	long	k+a	1.1	-11.5	6.4	2.8	0.94	0.16	0.13	-18.46
* 2419	25.15	23.50	22.45	20.96	0.7566	4	12.82	0.7	k	5.0	3.8	-12.9	-13.4	0.49	0.57	0.00	-21.30
* 2452	24.25	22.49	21.46	19.96	0.7580	4	12.66	0.7	k	5.0	-0.9	2.3	5.8	0.35	0.44	0.20	-22.30
* 2453	25.79	23.66	22.65	21.15	0.7522	4	12.71	0.7	k	5.0	0.2	5.0	1.3	0.33	0.45	0.00	-21.07
* 2527	24.87	23.14	21.87	20.23	0.7552	4	14.03	0.2	k	8.0	-2.4	7.0	-0.2	0.38	0.47	0.38	-21.97
2547	22.81	21.56	20.74	19.09	0.0000	4	13.40
2582	23.05	22.82	22.55	22.43	0.6910	4	2.69	long	a	0.8	-75.5	-25.9	-59.1	0.49	0.16	4.32	-20.16
2609	25.70	24.81	23.80	22.13	0.5832	3	13.70	0.3	k	6.0	-10.0	-0.2	6.5	0.04	0.03	0.09	-18.93
* 2611	24.47	24.30	24.07	22.39	0.7628	4	8.29	1.4	k	2.4	-9.2	17.1	19.6	0.53	0.37	0.27	-19.79
* 2657	23.28	22.77	22.42	21.60	0.7663	4	6.07	2.0	k+a	1.9	-28.1	-6.7	-10.9	0.59	0.23	2.60	-20.95
2661	24.91	24.88	24.12	22.99	0.7834	3	7.42	1.5	k+a	2.4	-87.5	0.52	0.09	1.92	-19.50
2666	23.57	22.82	22.66	22.06	0.4549	4	4.96	10.0	a+k	1.4	-43.6	-5.3	-16.5	0.52	0.25	0.70	-19.04
* 2684	23.43	23.01	22.72	21.85	0.7654	1	5.62	2.0	a	1.7	-39.9	-14.6	-23.5	0.37	0.10	2.86	-20.65
2708	20.70	20.15	19.76	19.54	0.0000	4	4.18
* 2747	26.65	23.65	22.83	21.28	0.7486	4	13.00	0.4	k	6.0	-0.8	0.9	9.4	0.61	0.51	0.05	-20.92
2843	24.28	23.89	23.30	22.36	0.7292	4	7.19	1.7	a	2.2	-58.9	0.37	-0.06	2.06	-19.94
2871	23.62	23.35	22.97	22.60	0.6961	4	3.87	long	a	1.1	-86.0	-7.8	-63.4	0.41	0.01	3.43	-19.84
2900	23.82	23.58	23.20	22.77	0.9848	3	3.89	1.7	...	1.8	-37.3	0.50	0.28	3.65	-20.99
* 2921	25.27	23.72	22.74	21.39	0.7564	4	11.66	0.9	k	4.0	1.9	11.7	-7.3	0.45	0.48	0.00	-20.91
* 2932	26.38	24.66	23.76	22.80	0.7552	4	9.09	1.4	k+a	3.0	-3.5	2.7	-13.7	0.34	0.32	0.09	-19.68
2943	23.77	22.55	21.62	20.79	0.4684	4	8.27	1.2	k+a	4.0	-5.7	-2.3	1.4	0.19	0.17	0.17	-20.08
* 3032	25.64	23.99	23.42	21.75	0.7618	4	13.30	0.7	k+a	5.0	2.6	10.5	1.7	0.57	0.37	0.00	-20.47
3083	25.25	24.28	23.22	21.53	1.0770	4	14.12	0.5	k	5.0	-0.3	0.96	0.59	0.00	-22.47
3103	23.71	23.55	23.29	22.88	1.1387	4	2.89	0.5	...	1.7	-58.4	0.60	0.20	8.07	-21.44

Table 2—Continued

ID#	AB_B	AB_V	AB_R	AB_I	z	Q	b	tau	Sp	Age		[OII]	$H\beta$	[OIII]	J_l	J_u	SFR	M_{ABB}
										$\tau_{0.6}$	$\tau_{0.6}$							
3114	24.48	23.15	22.37	21.14	0.6440	4	10.65	1.0	k	4.0	1.5	2.3	3.7	0.46	0.42	0.00	-20.55	
3125	24.23	22.99	22.15	20.68	0.0000	4	12.25	
3132	23.97	22.45	21.49	19.44	0.0000	4	16.93	
3142	22.81	22.03	21.76	21.54	0.2320	4	4.31	20.0	...	1.6	...	0.3	-4.9	0.07	-18.13	
3194	23.80	23.36	23.18	22.99	0.1270	1	3.16	5.0	...	1.3	...	0.0	39.0	0.00	-15.31	
3201	24.20	23.61	23.06	22.44	0.6446	4	6.30	2.0	a+k	1.9	-23.0	-2.4	-8.1	0.82	0.34	0.66	-19.61	
3214	21.01	20.00	19.66	19.20	0.0000	4	6.27	
3219	22.99	22.15	21.34	20.56	0.6192	4	7.87	1.7	a	2.6	-11.2	4.2	-2.9	0.80	0.31	1.29	-21.25	
3241	23.15	22.40	21.71	20.86	0.6586	4	7.89	1.7	a	2.4	-45.3	-16.7	-62.4	0.45	0.15	4.76	-21.11	
3260	24.15	24.28	23.48	22.74	0.8172	4	5.23	2.0	a+k	1.7	0.66	0.22	...	-20.08	
3277	23.63	23.23	22.82	22.66	0.4884	4	4.12	long	k+a	1.0	...	-11.2	-39.3	...	0.19	1.01	-18.95	
3329	24.08	23.33	22.91	22.57	0.0000	1	5.29	
3333	25.17	24.85	22.43	20.95	0.4874	4	12.68	...	k	8.0	...	-2.7	-1.7	...	0.25	0.12	-19.53	
3416	19.57	19.12	18.54	18.38	0.0000	4	4.42	
* 3505	23.48	22.63	21.94	20.75	0.7494	4	9.84	1.2	k+a	3.2	-18.2	-4.7	0.5	0.50	0.30	2.50	-21.58	
3526	24.53	23.39	23.27	22.87	0.5654	1	4.61	long	...	1.3	1.6	8.0	-5.2	0.51	0.51	0.00	-18.96	
3536	24.59	23.55	22.57	21.23	0.7260	1	11.48	0.9	a+k	4.0	-5.0	-16.1	-19.1	0.65	0.45	0.34	-20.91	
3556	25.16	24.63	23.52	22.31	0.7010	3	10.39	1.2	k+a	3.5	-16.1	0.86	0.14	0.40	-19.72	
3606	24.21	23.85	23.57	22.26	0.7013	4	7.60	1.7	a+k	2.2	-43.9	-12.1	-35.9	0.71	0.02	1.27	-19.70	
* 3632	27.61	25.78	24.96	22.87	0.7576	0	16.80	2.0	...	4.0	-34.8	0.41	...	-19.20	
* 3651	23.33	22.26	21.40	20.00	0.7513	4	11.68	0.9	k+a	4.0	-2.5	5.7	-1.7	0.66	0.34	0.59	-22.25	
3662	23.16	22.72	22.17	22.14	0.6424	4	4.73	long	a+k	1.4	-29.5	0.1	-19.4	0.69	0.35	1.87	-20.39	
3699	21.87	21.44	21.30	21.40	0.2124	4	2.54	long	...	0.8	...	5.6	-1.0	0.02	-18.54	
3724	22.74	22.06	21.53	21.02	0.4535	4	6.10	2.0	a+k	1.9	-14.2	-0.9	-1.7	0.61	0.24	0.54	-20.08	
* 3822	24.41	23.18	22.30	21.00	0.7576	4	11.20	0.9	k	3.8	-0.7	2.8	-1.6	0.50	0.35	0.07	-21.33	
3838	25.12	23.89	22.99	22.13	0.4889	4	8.61	1.2	a	3.8	-16.5	0.2	-7.7	0.30	0.06	0.16	-18.84	
3839	23.30	22.50	21.75	20.86	0.5948	4	8.23	1.6	k+a	2.8	-14.5	1.1	-6.3	0.66	0.31	1.01	-20.74	
3849	23.99	23.44	23.49	22.50	1.0799	3	4.98	1.2	...	2.0	-13.6	0.72	0.21	1.61	-21.27	
3874	22.68	22.02	21.52	21.22	0.4595	4	5.16	5.0	k+a	1.6	-37.6	-8.6	-11.3	0.57	0.19	1.57	-20.10	
3933	23.81	23.44	23.12	22.76	1.0750	2	3.95	1.6	...	1.8	-19.2	2.64	-21.38	
3955	22.87	22.94	22.90	22.51	1.2002	4	0.58	long	...	0.9	-124.9	0.77	0.53	23.68	-21.68	
3968	23.46	23.52	23.42	22.92	1.2002	4	1.00	5.0	a	1.3	-103.5	1.39	0.50	13.46	-21.34	
3979	24.70	24.34	23.62	22.86	0.5971	4	6.80	2.0	a	2.0	-88.6	-4.5	-37.9	...	0.33	1.18	-18.82	
4006	23.69	23.44	23.13	22.57	0.6898	4	3.95	long	k+a	1.1	-52.6	-7.2	-31.9	0.31	0.29	1.83	-19.69	
4046	24.10	23.52	23.28	22.92	0.3222	4	4.21	long	...	1.3	-24.9	0.10	-17.47	
* 4061	25.21	23.24	22.42	21.07	0.7556	4	11.51	0.9	k	4.0	-0.4	1.0	-0.2	0.57	0.49	0.00	-21.23	
* 4097	24.86	23.83	23.28	22.13	0.7524	3	9.44	1.2	a+k	3.0	-22.3	12.0	0.5	0.98	0.48	0.91	-20.21	
4113	24.10	23.82	24.08	23.07	9.0000	0	2.88	
4159	23.78	23.28	23.14	23.26	0.4446	4	3.01	long	a	0.6	...	-16.1	-116.9	1.85	-18.42	
4168	25.04	24.44	23.77	22.96	0.6583	1	7.44	1.9	...	2.4	-64.8	1.02	-19.05		
4191	0.1950	4	0.03	long	-1.0	-7.3		
4219	23.75	23.47	23.19	22.80	0.7024	4	3.47	long	k+a	1.0	-42.9	-1.0	-19.6	0.58	0.15	1.46	-19.64	
4283	26.76	23.75	23.17	22.66	0.6191	4	5.68	5.0	a	1.7	-60.7	1.3	-40.2	0.94	0.49	1.36	-19.33	
4305	24.47	22.86	21.99	20.62	0.6959	4	11.58	1.0	k	4.0	-3.0	7.3	1.5	0.49	0.41	0.31	-21.31	
4354	22.38	21.79	21.62	21.35	0.1940	4	3.69	long	...	1.4	...	-8.2	-31.7	0.37	-17.88	
* 4439	22.12	21.77	23.40	22.81	0.7705	4	-1.40	long	k+a	0.1	-58.5	-2.1	-62.8	0.89	0.31	6.44	-20.63	
4451	26.65	24.52	23.53	22.03	0.6492	4	12.92	0.4	k	5.0	-2.3	1.4	8.9	0.44	0.23	0.04	-19.55	
* 4469	21.70	21.73	21.65	21.31	0.7706	4	0.99	long	a	0.3	-60.7	-21.9	-42.4	0.44	0.13	11.02	-21.30	
4470	24.00	23.69	23.30	22.82	0.6430	4	4.35	long	a	1.3	-43.2	-30.2	-6.8	0.62	0.25	1.03	-19.29	
4572	22.49	21.72	24.12	24.13	0.5289	1	3.30	long	...	1.6	-40.5	2.95	-20.66		
4595	22.82	21.90	21.23	20.87	0.4223	4	6.02	2.0	a+k	2.4	...	-0.5	-3.2	...	0.30	-20.11		
4614	23.68	23.74	21.21	20.38	0.4197	4	8.05	0.2	k+a	10.0	-3.0	0.6	0.1	0.59	0.29	0.07	-20.06	

Table 2—Continued

ID#	AB_B	AB_V	AB_R	AB_I	z	Q	b	tau	Sp	Age		H β	[OIII]	J_l	J_u	SFR	M_{ABB}
										$\tau_{0.6}$	[OII]						
4632	22.63	22.31	22.24	22.04	9.0000	0	2.19
4658	24.48	23.71	22.99	22.65	0.4410	4	6.08	2.0	k+a	2.2	-35.2	0.1	-7.8	0.74	0.36	0.29	-18.49
4697	24.44	23.54	22.76	21.86	0.6165	4	8.61	1.5	k+a	3.0	-21.0	-5.2	-7.3	0.43	0.15	0.65	-19.86
4701	23.67	22.90	22.19	21.83	0.4673	4	6.03	2.0	a	2.2	-24.4	-2.4	-24.4	0.75	0.22	0.51	-19.46
4736	22.95	21.70	20.75	19.95	0.4219	4	8.30	1.0	k	5.0	-0.1	3.6	0.4	...	0.49	0.00	-20.58

Table 3. Photometric and Spectroscopic Data for Field CL1604+4304

ID#	AB_B	AB_V	AB_R	AB_I	z	Q	b	tau	Sp	Age	[OII]	$H\beta$	[OIII]	J_l	J_u	SFR	M_{ABB}
										$\tau_{0.6}$							
33	24.10	23.75	23.77	23.16	9.0000	0	2.89
68	23.25	22.29	21.89	21.08	0.3459	1	8.07	2.0	k+a	2.4	...	-4.9	-0.7	...	0.02	0.00	-18.96
99	23.79	23.49	22.68	21.26	0.8216	2	8.25	1.0	a	2.8	-38.9	6.2	1.5	0.41	0.07	3.83	-21.18
100	22.67	22.30	21.75	21.16	0.6825	4	5.50	1.8	a	1.9	-20.4	-1.0	-14.3	0.69	0.31	2.31	-21.13
130	24.72	24.30	24.04	22.16	0.4258	4	8.08	2.0	...	2.6	...	-4.1	-26.3	0.39	-18.04
178	25.14	24.16	23.85	21.96	0.9748	2	10.99	0.8	...	3.8	-57.7	0.49	0.22	5.78	-21.32
195	23.64	23.48	23.20	21.85	0.9738	2	4.57	1.2	...	2.2	-77.9	9.68	-21.33
205	23.71	22.66	21.96	20.88	0.3018	4	10.25	1.5	...	4.0	...	-6.6	-4.1	0.09	-18.37
208	25.30	24.11	23.53	21.64	0.8074	4	12.99	0.9	k+a	4.0	-7.8	-8.0	-3.8	0.72	0.40	0.42	-20.69
233	23.65	23.18	22.77	21.67	0.4965	4	6.20	5.0	a+k	1.7	-60.3	-8.3	-20.4	0.90	0.34	1.14	-19.28
252	...	25.78	23.83	22.04	9.0000	0
* 256	23.55	23.45	23.19	21.78	0.8938	3	4.18	1.5	a	1.9	-73.7	17.4	-30.7	0.32	0.08	6.63	-20.95
319	23.32	22.63	22.45	21.60	0.1893	4	6.00	10.0	...	1.7	...	-0.7	-17.1	0.09	-16.97
327	23.21	22.99	22.62	21.48	0.8720	4	4.60	1.5	a+k	2.0	-71.5	0.7	3.3	0.35	0.14	9.19	-21.36
332	24.69	23.90	23.50	22.17	0.2980	4	8.52	2.0	a+k	3.0	...	8.0	-15.3	0.10	-17.07
471	24.06	23.05	22.61	21.87	0.3839	2	8.40	2.0	...	2.6	1.7	-1.1	-2.1	...	0.17	0.00	-18.53
491	26.19	24.17	23.25	21.18	1.0905	1	16.65	0.4	...	5.0	-7.7	2.40	-22.72
544	23.68	22.36	21.64	20.59	0.3891	4	10.92	1.2	a+k	5.0	-9.6	4.4	-3.1	0.66	0.46	0.15	-19.48
600	24.77	24.18	23.95	22.44	9.0000	0	7.35
634	24.40	24.08	23.43	21.90	1.2316	2	8.01	0.5	...	4.0	-56.2	0.59	0.34	20.96	-22.87
636	24.51	23.77	23.12	21.67	0.8288	4	9.86	1.0	a+k	3.5	-5.0	-8.1	-2.7	0.29	0.18	0.38	-21.01
642	24.61	23.88	23.44	22.55	0.3142	4	7.33	5.0	...	2.2	...	-8.5	-33.6	0.22	-17.19
656	22.70	22.29	21.84	21.33	0.4954	4	5.16	20.0	a	1.3	-59.7	-14.1	-63.3	...	0.23	2.43	-20.02
681	23.11	22.32	22.13	21.55	0.2733	4	6.31	10.0	...	1.6	...	-1.3	-9.7	0.15	-18.21
858	25.20	24.11	23.14	20.95	0.8280	0	16.04	0.6	k	5.0	-13.2	-2.4	0.7	0.38	0.51	1.29	-21.43
931	24.73	23.83	22.99	21.32	0.8329	2	12.24	0.8	k+a	4.0	-3.8	1.9	3.5	0.40	0.14	0.34	-21.26
944	23.78	23.39	23.34	21.96	0.9742	3	4.96	1.2	a+k	2.2	-37.4	0.52	0.25	4.32	-21.25
950	23.61	23.35	23.20	22.41	9.0000	0	3.17
971	22.49	22.02	21.47	20.87	0.4998	4	6.20	5.0	k+a	1.6	-52.3	0.7	-6.8	2.87	-20.39
* 1025	23.57	23.05	22.75	21.36	0.8798	4	6.87	1.2	a+k	2.8	-29.0	-5.8	-45.0	0.21	0.09	4.00	-21.55
1055	24.03	23.77	23.18	22.08	0.5479	4	5.97	2.0	a+k	1.7	-131.5	2.6	-98.1	-0.25	0.03	2.24	-19.10
* 1059	24.51	24.02	23.68	22.19	0.8804	2	7.21	1.0	k+a	2.8	-14.2	-3.8	-10.1	0.33	0.22	0.83	-20.62
1133	26.30	23.91	22.79	20.83	0.8707	2	16.64	0.3	...	7.0	-88.3	10.1	-16.3	0.90	0.58	12.72	-22.00
1138	24.52	24.25	23.54	21.83	9.0000	0	8.66
1178	24.73	24.94	24.16	22.04	0.7787	1	8.43	1.3	...	2.8	-92.8	2.99	-19.96
1205	24.04	24.19	23.65	22.23	1.0966	4	4.36	1.0	a	2.6	-48.2	0.21	0.01	6.39	-21.50
1207	23.62	23.09	22.76	22.01	0.4909	2	5.54	5.0	a+k	1.6	...	0.4	-5.3	0.20	-19.21
1250	24.09	23.16	23.17	22.01	0.2405	4	6.95	5.0	...	2.0	...	-4.7	-15.6	0.09	-17.02
* 1267	23.37	22.79	22.02	20.63	0.8984	4	9.42	1.0	k+a	3.5	-8.0	16.0	7.2	0.53	0.29	2.22	-22.42
1270	25.29	23.73	23.78	21.29	0.4964	2	13.65	0.1	...	8.0	-90.8	-3.6	10.7	...	0.02	0.99	-19.22
1289	25.33	24.15	23.75	21.37	0.8294	4	14.41	0.7	k+a	4.0	-0.3	3.5	10.1	0.63	0.33	0.00	-20.91
1311	24.20	23.76	23.92	22.00	9.0000	0	6.38
1374	24.24	23.89	23.07	22.58	0.4142	3	6.84	5.0	a+k	1.7	-18.7	4.8	-5.9	0.41	0.23	0.14	-18.20
* 1392	...	28.85	24.59	21.48	0.8968	2	...	long	a+k	...	-16.6	6.8	16.2	0.35	0.04	0.00	...
* 1399	24.12	23.70	23.55	21.79	0.8893	1	7.07	1.2	k+a	2.6	-35.0	20.9	-2.8	0.50	0.26	2.80	-20.95
1417	26.20	25.58	23.62	21.26	1.0682	2	19.20	0.2	...	6.0	-37.0	0.24	-0.23	8.81	-22.55
* 1444	25.47	24.79	23.28	21.39	0.8998	4	15.26	0.6	k	5.0	2.1	9.2	-5.7	0.16	0.33	0.00	-21.50
* 1495	23.14	22.85	22.54	21.56	0.9005	2	4.31	1.5	...	2.2	-37.9	0.24	-0.03	6.08	-21.64
1506	25.82	24.46	24.09	22.21	0.3796	2	12.38	0.4	k	5.0	...	6.9	-0.4	0.00	-17.38
* 1603	24.57	23.46	22.36	20.80	0.8956	4	13.71	0.7	k	4.0	1.2	-5.6	-2.4	0.36	0.46	0.00	-22.10
1606	21.27	19.95	19.49	18.69	0.2415	4	8.95	1.5	...	5.0	...	3.8	1.6	0.00	-20.29
1642	23.94	23.18	22.93	22.03	0.4779	2	6.69	2.0	k+a	2.0	...	1.5	-1.0	0.00	-19.06

Table 3—Continued

Table 3—Continued

ID#	AB_B	AB_V	AB_R	AB_I	z	Q	b	tau	Sp	Age		$[OIII]$	J_l	J_u	SFR	M_{ABB}	
										$\tau_{0.6}$	[OII]						
3730	24.01	23.26	22.68	21.46	0.4713	4	8.83	2.0	k+a	2.8	-12.0	1.0	-1.8	...	0.30	0.19	-19.21
3736	23.94	23.44	22.69	22.04	0.6394	4	7.43	1.5	a+k	2.4	-11.3	0.0	-0.1	0.52	0.24	0.42	-20.00
3760	23.77	23.21	22.66	21.19	0.7804	4	8.54	1.1	k+a	3.0	-32.2	-15.5	2.3	0.63	0.19	2.92	-21.11
3782	25.29	24.49	24.26	22.06	0.7790	1	11.23	0.9	...	3.5	-56.5	1.76	-20.03
3821	25.65	24.11	23.55	21.10	9.0000	0	16.71
3906	1.0571	1	5.5	0.0	0.0
3907	0.5987	3	k+a	...	-13.4	-10.2	-2.9	0.48	0.32
3908	0.1894	4	-2.9	-3.2
3909	0.2551	4	4.1	-3.1
3910	0.5991	2	a+k	...	2.9	-2.4	-18.7	0.00	0.02
3911	0.3778	4	k+a	...	-0.4	-1.2
3912	0.4957	4	k	...	0.6	3.9	2.0	...	0.52

Note. — Two spectroscopically confirmed members of CL1604+4304 lie near the edge of our LRIS imager and, hence, only have photometric information for the R-band. These two galaxies are not included in Table 3 but their redshifts are 0.9040 and 0.9073

Table 4. Photometric and Spectroscopic Data for Field CL1604+4321

ID#	AB_B	AB_V	AB_R	AB_I	z	Q	b	tau	Sp	Age	[OII]	$H\beta$	[OIII]	J_l	J_u	SFR	M_{ABB}
										$\tau_{0.6}$							
173	24.38	24.25	24.36	23.08	9.0000	0	2.47
181	34.96	24.44	23.65	22.07	0.6956	4	13.36	0.5	k	6.0	2.0	7.1	9.8	0.53	0.35	0.00	-19.79
217	23.93	23.87	23.64	23.24	9.0000	0	1.70
244	25.08	24.32	24.05	24.07	0.4599	2	5.98	20.0	...	1.6	...	-2.9	-5.7	0.05	-17.70
259	23.91	23.28	22.80	23.28	0.3464	4	6.46	10.0	a+k	1.6	-64.7	-21.2	-54.6	...	0.49	0.42	-17.98
367	22.98	21.73	20.90	19.22	0.0000	4	13.34
432	24.04	23.91	23.80	23.25	9.0000	0	1.77
443	23.24	23.08	23.13	23.33	9.0000	0	1.00
474	24.23	23.96	23.73	22.69	1.1768	4	4.13	0.8	...	2.8	-32.0	4.76	-21.70
486	23.90	23.88	22.35	22.17	1.1760	4	9.07	0.6	...	4.0	-44.2	26.95	-23.39
608	22.84	23.09	22.62	20.59	0.8647	4	6.26	1.5	k+a	2.2	-36.5	-5.1	-5.7	0.75	0.45	6.80	-21.80
609	23.44	23.21	23.26	23.09	0.8652	4	1.60	long	a	1.0	-67.7	-2.8	...	0.41	0.15	4.48	-20.45
625	23.06	23.47	21.66	20.11	0.3022	4	10.18	0.2	k	4.0	...	2.3	1.5	0.00	-18.69
653	0.8650	4	-99.2	0.15	-0.05	
688	22.42	22.62	21.75	20.02	0.8081	4	7.71	1.3	a+k	2.4	-20.9	0.29	0.03	5.11	-22.11
704	24.71	23.80	23.11	22.39	0.4978	4	9.10	1.7	k+a	3.0	...	5.4	-3.5	...	0.69	0.11	-18.81
714	21.66	20.86	20.46	19.75	0.1308	4	6.71	5.0	...	3.5	...	0.9	-2.5	0.04	-17.74
764	24.17	23.66	23.70	22.89	1.2835	2	4.01	0.7	...	3.0	-9.4	2.22	-22.29
769	24.56	23.05	23.91	22.37	0.7750	4	6.97	1.1	k+a	3.0	-4.0	-8.8	-22.4	0.55	0.37	0.31	-20.90
813	23.89	22.94	22.94	22.33	9.0000	0	6.14	
849	25.25	24.20	23.44	23.67	0.4291	4	10.06	1.7	a+k	3.2	...	-9.1	-45.3	0.64	-17.95
897	23.71	24.22	23.39	21.69	0.7267	1	5.07	2.0	...	1.7	-74.2	-4.9	-66.5	0.36	0.09	3.18	-20.09
913	25.68	22.92	21.89	20.29	0.7910	4	14.17	0.2	k	7.0	0.4	10.4	-18.0	0.49	0.45	0.00	-22.18
* 942	24.20	23.90	23.69	23.25	0.9232	2	3.23	1.8	...	1.8	-82.0	0.40	0.42	4.53	-20.40
963	25.06	23.72	22.91	21.20	0.6196	4	13.52	0.6	k	6.0	-2.6	8.1	2.7	0.99	0.47	0.08	-20.06
968	25.12	25.78	24.59	23.65	9.0000	0	3.67	
1007	21.22	20.54	19.93	19.37	0.4668	4	6.71	2.0	k+a	2.2	-15.1	0.4	-2.0	...	0.56	2.70	-21.79
1050	24.05	23.79	23.82	23.55	9.0000	0	1.96	
1086	24.38	24.21	24.17	23.53	0.8017	1	1.95	long	...	1.0	-71.6	1.9	-4.8	0.22	-0.03	1.61	-19.26
1096	24.16	23.40	22.68	22.24	0.4664	4	8.55	2.0	a	2.4	-30.3	-10.1	-8.9	...	0.28	0.39	-18.97
* 1116	25.57	24.31	22.95	21.71	0.9232	4	13.55	0.6	k+a	5.0	-23.5	0.66	0.22	3.04	-21.72
* 1178	24.43	24.70	23.61	23.85	0.9189	2	4.28	1.2	...	2.2	-60.4	0.33	0.12	3.12	-20.40
1182	23.87	22.86	23.25	22.33	9.0000	0	5.77	
1192	24.86	24.70	23.50	23.84	0.4844	4	7.98	2.0	k+a	2.2	-81.1	-2.9	-7.2	0.51	-18.17
1264	23.68	22.86	22.82	21.54	1.1008	4	6.80	0.8	...	3.0	-22.2	0.47	0.10	7.28	-22.53
** 1292	23.13	22.64	22.44	20.33	0.9347	2	9.33	0.9	a	3.2	-32.4	0.30	0.06	10.38	-22.52
1293	25.00	23.53	22.67	21.74	1.0274	4	11.52	0.7	k	4.0	-13.2	0.72	0.28	3.61	-22.47
* 1317	23.97	23.52	23.54	22.77	0.9182	3	3.68	1.8	a+k	1.9	-53.3	0.31	0.14	3.90	-20.73
1328	24.60	24.36	24.24	24.17	9.0000	0	2.20	0.01	...	
1339	23.26	22.75	22.11	20.46	2.4970	4	9.66	3.0	
1353	24.45	24.20	24.50	24.38	9.0000	0	1.10	
1632	22.90	22.40	22.24	22.50	0.1311	4	4.18	long	...	1.3	...	28.2	24.1	0.00	-16.30
1699	23.10	23.05	23.15	23.44	1.1751	4	-0.04	long	...	0.5	-14.1	1.71	-21.05
* 1722	25.24	24.30	23.58	22.24	0.9175	4	10.68	0.8	a+k	3.8	-15.5	0.80	0.32	1.14	-21.01
1828	24.62	24.32	24.28	21.71	9.0000	0	10.20	
1830	24.65	24.17	24.26	26.99	9.0000	0	3.28	
* 1897	23.61	23.29	22.98	21.74	0.9190	4	5.34	1.2	a	2.2	-29.4	-13.0	...	0.43	0.21	3.39	-21.27
* 1903	23.58	23.47	23.45	22.22	0.9188	2	2.74	2.0	...	1.4	-57.4	4.36	-20.67
1911	24.99	24.61	23.91	24.12	0.8223	2	6.13	1.2	...	2.4	-63.4	-21.1	...	0.67	0.28	1.78	-19.76
1947	25.27	24.29	23.56	21.08	9.0000	0	16.48	
1982	24.56	24.05	23.71	23.57	0.7263	4	5.00	1.7	a	2.0	-56.7	-7.1	-24.2	0.72	0.33	1.37	-19.50
* 2012	25.39	24.58	24.61	22.95	0.9247	1	7.84	0.9	...	3.0	0.2	0.00	-20.20

Table 4—Continued

ID#	AB_B	AB_V	AB_R	AB_I	z	Q	b	tau	Sp	Age	[OII]	$H\beta$	[OIII]	J_l	J_u	SFR	M_{ABB}
										$\tau_{0.6}$							
* 2032	25.23	24.64	24.06	22.33	0.9185	2	10.07	0.9	...	3.5	-31.0	0.71	0.30	1.68	-20.64
2051	23.99	23.23	23.02	22.76	9.0000	0	5.96
2058	23.86	23.75	23.57	23.25	9.0000	0	1.74
* 2079	26.84	25.30	23.90	21.84	0.9220	4	17.68	0.2	k+a	5.0	-1.4	0.40	0.27	0.10	-21.23
* 2120	25.64	24.08	23.06	21.12	0.9274	4	15.95	0.5	k	5.0	1.4	0.65	0.62	0.00	-21.90
* 2140	24.26	23.75	23.38	21.95	0.9232	4	7.39	0.9	a+k	2.8	-19.3	0.64	0.28	1.74	-21.09
* 2153	25.24	24.29	23.40	22.51	0.9250	4	10.43	0.8	k	3.8	-2.9	-17.4	18.1	0.75	0.54	0.24	-21.11
* 2204	24.25	23.61	22.95	21.68	0.9264	4	9.04	0.9	k	3.5	-6.5	0.55	0.46	0.88	-21.63
2220	24.36	24.06	23.68	22.74	1.1818	3	4.80	0.8	...	3.0	-35.0	5.37	-21.76
2253	23.94	23.89	23.80	24.54	1.2773	2	1.17	1.0	...	1.9	-21.54
2289	...	25.09	23.92	22.41	9.0000	0
2308	24.27	23.74	23.18	22.93	0.4889	4	6.32	5.0	a	1.7	-33.4	-7.1	-11.3	0.85	0.18	0.35	-18.65
2362	24.25	23.75	24.04	24.17	9.0000	0	3.04
2365	23.70	23.42	22.98	22.39	0.7262	4	4.38	2.0	a	1.7	-53.0	-3.0	-40.1	0.46	0.10	2.42	-20.16
* 2368	25.05	24.59	24.41	23.27	0.9205	4	5.34	1.4	a	2.2	-13.0	0.28	0.16	0.42	-19.88
2380	25.16	24.52	23.90	21.88	1.0988	4	11.92	0.6	k	4.0	-17.2	0.76	0.47	2.77	-21.91
* 2434	25.91	24.58	23.48	21.76	0.9228	4	14.85	0.6	k+a	5.0	1.5	0.38	0.35	0.00	-21.34
* 2458	26.00	24.29	23.35	21.83	0.9192	3	13.60	0.6	k	5.0	0.2	-7.9	15.6	0.59	0.43	0.00	-21.43
* 2491	23.83	23.31	22.97	21.90	0.9344	4	6.11	1.1	a	2.8	-17.1	0.43	0.17	2.25	-21.48
2494	24.54	24.87	23.18	22.40	0.6954	4	8.26	1.4	a	2.6	-45.3	-11.1	-31.4	0.63	0.22	1.36	-19.81
* 2542	23.94	23.68	23.48	22.50	0.9172	2	3.79	1.7	k	1.9	-44.6	0.40	0.26	3.15	-20.69
* 2603	24.83	23.97	23.37	21.55	0.9379	3	11.81	0.8	k+a	4.0	-2.9	-14.1	8.4	0.46	0.50	0.36	-21.58
* 2613	24.89	24.45	24.12	22.86	0.9181	3	6.25	1.2	k+a	2.4	-36.5	-9.3	...	0.35	0.17	1.50	-20.19
* 2666	25.06	24.21	23.84	22.05	0.9222	4	10.44	0.8	a+k	3.5	-2.6	0.65	0.31	0.19	-20.95
* 2670	25.77	24.10	23.14	21.28	0.9245	4	15.35	0.6	k	5.0	2.3	0.41	0.42	0.00	-21.76
2697	24.46	23.71	23.37	22.69	0.5100	4	6.57	2.0	a	1.9	-36.7	3.0	-42.9	0.44	0.20	0.41	-18.71
2739	23.32	22.60	21.87	20.70	0.6938	4	9.32	1.2	a+k	3.0	-267.7	-2.3	-13.4	0.53	0.19	...	-21.24
* 2775	24.16	23.61	23.21	22.16	0.9239	1	6.49	1.2	a	2.8	-7.8	-12.4	2.1	0.51	0.17	0.77	-21.19
2882	23.46	23.29	22.76	21.66	1.1742	4	5.22	0.8	...	3.0	-58.4	20.76	-22.65
3065	24.61	24.31	24.16	23.41	0.2416	4	4.21	long	...	1.3	...	-12.2	-28.6	1.54	-19.63
3087	24.42	23.14	22.78	22.31	0.2419	4	8.09	2.0	...	3.2	...	-6.4	-27.7	0.17	-17.04
* 3097	24.08	24.03	23.60	23.38	0.9333	4	2.45	1.9	a+k	1.7	-58.3	0.59	0.14	3.34	-20.42
* 3130	24.71	24.37	23.91	23.39	0.9288	4	4.77	1.2	a	2.4	-13.2	0.28	0.19	0.61	-20.30
* 3188	25.69	24.81	23.21	21.57	0.9206	4	15.17	0.5	k+a	5.0	-15.4	0.4	-6.3	0.67	0.33	1.66	-21.53
* 3199	26.37	24.67	23.66	21.99	0.9192	3	14.57	0.5	k	5.0	-5.8	0.53	0.43	0.44	-21.13
* 3218	26.31	24.53	23.58	21.93	0.9212	4	14.33	0.5	k+a	5.0	-1.8	0.48	0.42	0.15	-21.23
3240	24.14	23.34	22.86	22.08	0.2414	4	7.64	5.0	...	2.4	...	-1.9	-1.3	0.01	-17.00
* 3251	23.56	22.58	22.15	21.12	0.9222	4	8.57	0.9	a+k	3.2	-7.5	0.16	0.10	2.03	-22.35
3294	24.88	23.94	23.68	23.01	0.4548	1	7.01	5.0	...	2.0	...	-10.9	-24.8	...	0.28	0.35	-18.11
* 3312	25.08	24.23	23.91	22.82	0.9347	3	7.68	0.9	...	3.0	-16.8	0.94	-20.59
* 3369	28.76	24.72	23.61	21.61	0.9334	4	16.83	0.2	k	7.0	2.0	0.43	0.43	0.00	-21.62
3430	23.98	23.37	23.28	0.6183	4	3.50	long	a	1.1	-60.6	-1.8	-77.1	0.57	0.34	1.27	-19.13	
3472	24.09	22.98	22.67	21.43	0.2130	1	8.77	2.0	...	4.0	21.4	11.7	-6.4	0.00	-16.89
* 3475	24.17	23.41	22.69	21.24	0.9227	4	10.41	0.9	k	3.5	-4.9	0.50	0.28	0.81	-21.86
* 3495	23.17	22.72	22.30	21.09	0.9211	4	6.55	1.2	k+a	2.6	-20.5	-20.9	...	0.36	0.27	4.63	-22.07
3509	23.26	22.93	22.62	21.75	0.0991	4	4.43	20.0	...	1.7	-15.22
3529	24.79	24.34	24.09	23.39	0.9802	2	4.65	1.1	...	2.4	-107.5	5.55	-20.41
3622	24.99	24.58	24.38	23.60	0.4560	4	4.31	20.0	k+a	1.0	-8.0	1.6	-1.6	0.32	0.35	0.03	-17.42
* 3635	24.62	23.70	23.31	21.98	0.9223	4	8.94	0.9	a	3.2	-28.8	0.78	0.34	2.86	-21.25
3674	23.74	22.55	21.67	20.66	0.4558	4	11.35	1.2	k+a	4.0	-9.1	2.7	-5.9	0.31	0.29	0.23	-19.97
3682	25.74	23.97	23.30	21.92	0.7152	4	11.72	0.9	a+k	4.0	-15.3	10.1	-4.7	0.70	0.37	0.53	-20.14
* 3737	25.67	24.11	23.08	21.64	0.9210	4	13.54	0.6	k	5.0	-19.6	0.49	0.50	2.42	-21.67

Table 4—Continued

Table 4—Continued

ID#	AB_B	AB_V	AB_R	AB_I	z	Q	b	tau	Sp	Age		$[OII]$	$H\beta$	$[OIII]$	J_l	J_u	SFR	M_{ABB}
										$\tau 0.6$	$\tau 0.6$							
5628	23.27	22.58	22.01	21.58	0.4663	4	7.34	5.0	k+a	2.0	...	3.4	-11.4	0.69	-19.68	
5629	24.35	24.28	24.15	23.81	0.6972	2	1.56	long	...	0.6	-20.8	-2.7	0.0	0.89	0.10	0.31	-18.62	
5637	24.47	23.15	22.36	20.73	0.7141	4	13.05	0.8	k+a	4.0	1.5	5.5	-0.8	0.11	0.10	0.00	-21.09	
5684	25.87	25.86	24.45	...	9.0000	0	
6019	26.04	24.65	23.76	22.70	0.8138	3	11.70	0.8	k	4.0	1.1	30.9	33.3	0.50	0.75	0.00	-20.20	
6127	24.36	24.19	23.47	23.35	0.6237	4	4.87	5.0	a+k	1.4	-18.93	
6133	23.48	22.30	21.35	19.80	0.0000	4	13.20	-0.7	-1.6	

Table 5. Cluster Dynamical Parameters

Cluster	N_z	\bar{z}	σ	M_{PW}	M_{PM} ($10^{14}h_{65}^{-1} M_\odot$)	M_{RW}	Radius (h_{65}^{-1} kpc)
CL1324+3011	16	0.7568	1037^{+258}_{-150}	$5.89^{+2.94}_{-1.71}$	7.48 ± 0.58	11.8 ± 0.92	385
CL1324+3011	24	0.7561	942^{+178}_{-115}	$8.15^{+3.11}_{-2.03}$	9.71 ± 0.49	13.8 ± 0.69	770
CL1324+3011	32	0.7565	1058^{+166}_{-114}	$13.9^{+4.37}_{-3.02}$	31.1 ± 2.49	28.0 ± 2.25	Unlimited
CL1604+4304	11	0.8964	921^{+303}_{-155}	$3.77^{+2.58}_{-1.46}$	6.48 ± 1.17	14.2 ± 2.57	385
CL1604+4304	19	0.8967	1300^{+286}_{-173}	$10.6^{+4.78}_{-3.03}$	42.0 ± 4.52	48.2 ± 5.18	770
CL1604+4304	22	0.8967	1226^{+245}_{-154}	$12.0^{+4.91}_{-3.23}$	38.9 ± 3.58	48.2 ± 4.43	Unlimited
CL1604+4321	17	0.9246	994^{+236}_{-140}	$5.08^{+2.54}_{-1.62}$	6.68 ± 0.72	11.6 ± 1.25	385
CL1604+4321	35	0.9243	922^{+137}_{-96}	$9.31^{+2.80}_{-2.00}$	13.9 ± 0.66	21.5 ± 1.03	770
CL1604+4321	41	0.9243	935^{+126}_{-91}	$11.8^{+3.22}_{-2.34}$	20.9 ± 1.35	24.9 ± 1.62	Unlimited

Table 6. Cluster Mass-to-Light Ratios

Cluster	Radius (h_{65}^{-1} kpc)	M_{PM}/L_B	M_{PM}/L_V	M_{PM}/L_R
CL1324+3011	385	347 ± 49	327 ± 85	527 ± 106
	770	285 ± 40	255 ± 66	416 ± 84
CL1604+4304	385	208 ± 90	144 ± 50	159 ± 54
	770	127 ± 28	134 ± 24	319 ± 58
CL1604+4321	385	248 ± 45	168 ± 47	500 ± 161
	770	96 ± 8	103 ± 14	365 ± 57

Table 7. Galaxy Luminosity Function Parameters (with $\alpha = -1.15$)

z range	\bar{z}	N_{gal}	M_{ABB}^* ($+5\log(h_{65})$)	ϕ^* ($h_{65}^3 \text{ Mpc}^{-3}$)	χ^2_ν	$\langle V/V_{\max} \rangle$
$0.1 \leq z < 0.5$	0.362	103	-20.35 ± 0.24	0.024	1.42	0.27
$0.5 \leq z < 0.7$	0.630	69	-20.80 ± 0.21	0.017	1.10	0.35
$0.7 \leq z \leq 1.0$	0.820	57	-21.15 ± 0.23	0.011	0.19	0.49
Cluster Members	0.859	91	-21.44 ± 0.17	...	2.83	0.43

Note. — Results for $0.7 \leq z \leq 1.0$ bin exclude the cluster members.

Table 8. Mean Spectral Properties of Distant Cluster Galaxies

Subset	\bar{b}	EW $\lambda 3835$	EW CaII K	EW g-band (Angstroms)	J_l	J_u	ABB
Blue ($b \leq 10$)	6.06 (± 0.36)	2.41 (± 0.41)	3.01 (± 0.52)	1.89 (± 0.57)	0.43 (± 0.03)	0.20 (± 0.02)	-20.83 (± 0.11)
Red ($b \geq 11$)	13.93 (± 0.31)	5.37 (± 0.48)	7.64 (± 0.30)	3.62 (± 0.41)	0.47 (± 0.02)	0.43 (± 0.01)	-21.53 (± 0.11)
Type “a”	4.96 (± 0.57)	1.88 (± 0.82)	1.92 (± 0.93)	1.69 (± 1.47)	0.39 (± 0.04)	0.15 (± 0.02)	-20.82 (± 0.21)
Type “a+k”	7.24 (± 0.79)	2.84 (± 0.57)	1.99 (± 0.48)	0.81 (± 0.34)	0.51 (± 0.07)	0.20 (± 0.03)	-20.93 (± 0.17)
Type “k+a”	10.22 (± 0.93)	3.55 (± 0.57)	5.14 (± 0.40)	2.04 (± 0.61)	0.50 (± 0.03)	0.30 (± 0.02)	-21.31 (± 0.16)
Type “k”	12.89 (± 0.53)	5.50 (± 0.53)	8.19 (± 0.30)	4.40 (± 0.37)	0.46 (± 0.02)	0.44 (± 0.01)	-21.50 (± 0.11)

Table 9. Predicted Evolution in BCG Luminosity: M_{ABB} vs z

z	$H_o = 65$			$H_o = 80$		
	tau0.2	tau0.6	tau1.0	tau0.2	tau0.6	tau1.0
0.033	-21.59	-21.59	-21.59	-21.59	-21.59	-21.59
0.190	-21.79	-21.81	-21.83	-21.79	-21.81	-21.86
0.320	-21.95	-21.97	-22.01	-21.94	-22.00	-22.08
0.490	-22.12	-22.17	-22.26	-22.13	-22.23	-22.40
0.620	-22.25	-22.31	-22.46	-22.26	-22.40	-22.65
0.760	-22.37	-22.47	-22.68	-22.41	-22.61	-22.91
0.840	-22.45	-22.56	-22.81	-22.50	-22.72	-23.06
0.900	-22.51	-22.64	-22.91	-22.56	-22.81	-23.16
1.100	-22.69	-22.90	-23.24	-22.73	-23.15	-23.50
1.300	-22.90	-23.24	-23.61	-22.83	-23.39	-23.70
1.500	-22.98	-23.41	-23.78	-23.05	-23.69	-23.94

Table 10. Mean Normalized Star Formation Rate vs Redshift ($M_{\odot} \text{ yr}^{-1} L_{ABB}^{-1}$)

z range	Luminosity range				SFRN(No. objects)			
	1	2	3	4	1	2	3	4
0.40-0.55	-18.11	-19.11	-20.11	-21.11	1.69 (23)	1.63 (21)	0.78 (5)	0.52 (1)
	-19.10	-20.10	-21.10	-22.10				
0.55-0.65	-18.28	-19.28	-20.28	-21.28	1.61 (9)	0.88 (18)	0.50 (11)	...
	-19.27	-20.27	-21.27	-22.27				
0.65-0.75	-18.41	-19.41	-20.41	-21.41	1.55 (6)	1.84 (19)	0.76 (9)	0.32 (2)
	-19.40	-20.40	-21.40	-22.40				
CL1324	-18.50	-19.50	-20.50	-21.50	2.46 (3)	0.63 (7)	0.75 (16)	0.15 (6)
$z = 0.76$	-19.49	-20.49	-21.49	-22.49				
0.75-0.85	-18.55	-19.55	-20.55	-21.55	2.40 (4)	1.18 (8)	0.87 (13)	0.24 (3)
	-19.54	-20.54	-21.54	-22.54				
0.85-0.95	-18.67	-19.67	-20.67	-21.67	...	2.96 (1)	1.82 (2)	0.98 (4)
	-19.66	-20.66	-21.66	-22.66				
CL1604	-18.69	-19.69	-20.69	-21.69	...	1.50 (12)	0.70 (31)	0.25 (15)
$z \approx 0.91$	-19.68	-20.68	-21.68	-22.68				
0.95-1.05	-18.83	-19.83	-20.83	-21.83	...	3.80 (1)	1.90 (6)	0.22 (3)
	-19.82	-20.82	-21.82	-22.82				
1.05-1.50	-19.09	-20.09	-21.09	-22.09	...	1.34 (3)	1.81 (15)	1.19 (14)
	-20.08	-21.08	-22.08	-23.08				